Springer Theses
Recognizing Outstanding Ph.D. Research

Zane Baird

Manipulation and Characterization of Electrosprayed Ions Under Ambient Conditions

Methods and Instrumentation

Springer

Springer Theses

Recognizing Outstanding Ph.D. Research

Aims and Scope

The series "Springer Theses" brings together a selection of the very best Ph.D. theses from around the world and across the physical sciences. Nominated and endorsed by two recognized specialists, each published volume has been selected for its scientific excellence and the high impact of its contents for the pertinent field of research. For greater accessibility to non-specialists, the published versions include an extended introduction, as well as a foreword by the student's supervisor explaining the special relevance of the work for the field. As a whole, the series will provide a valuable resource both for newcomers to the research fields described, and for other scientists seeking detailed background information on special questions. Finally, it provides an accredited documentation of the valuable contributions made by today's younger generation of scientists.

Theses are accepted into the series by invited nomination only and must fulfill all of the following criteria

- They must be written in good English.
- The topic should fall within the confines of Chemistry, Physics, Earth Sciences, Engineering and related interdisciplinary fields such as Materials, Nanoscience, Chemical Engineering, Complex Systems and Biophysics.
- The work reported in the thesis must represent a significant scientific advance.
- If the thesis includes previously published material, permission to reproduce this must be gained from the respective copyright holder.
- They must have been examined and passed during the 12 months prior to nomination.
- Each thesis should include a foreword by the supervisor outlining the significance of its content.
- The theses should have a clearly defined structure including an introduction accessible to scientists not expert in that particular field.

More information about this series at http://www.springer.com/series/8790

Zane Baird

Manipulation and Characterization of Electrosprayed Ions Under Ambient Conditions

Methods and Instrumentation

Doctoral Thesis accepted by
Purdue University, West Lafayette, USA

Springer

Author
Dr. Zane Baird
Department of Chemistry
Purdue University
West Lafayette, IN
USA

Supervisor
Prof. R. Graham Cooks
Department of Chemistry
Purdue University
West Lafayette, IN
USA

ISSN 2190-5053 ISSN 2190-5061 (electronic)
Springer Theses
ISBN 978-3-319-49868-3 ISBN 978-3-319-49869-0 (eBook)
DOI 10.1007/978-3-319-49869-0

Library of Congress Control Number: 2016957704

Printed on acid-free paper

This Springer imprint is published by Springer Nature
The registered company is Springer International Publishing AG
The registered company address is: Gewerbestrasse 11, 6330 Cham, Switzerland

To Gary, JoDi, Tess, and Tawni

Supervisor's Foreword

Zane Baird's thesis is a model of innovation combined with high technical achievement. These are characteristics one could wish to find in any STEM Ph.D. thesis but often does not. The subject Baird treats is mass spectrometry, but more broadly it is measurement science. This term implies the existence of measurement tools, and methods for testing and validating and interpreting the data from measurements. The subject of analytical chemistry has evolved to become that part of chemistry that is most concerned with the invention of new measurement tools, and the methodology of testing, validating and interpreting data. Baird's work covers a novel evolving area of mass spectrometry, in which ions are treated in the ambient environment. His experiments involve generation of ions in air, and more unusually, the focusing, separation and detection of ions in air. To accomplish this, he uses new rapid prototyping methods of 3D printing to fabricate lens systems which focus ions and create beams which can be reacted, separated and detected. These tasks are facilitated by simulations of ion motion. One novel result is the construction from plastic at low cost using a home hobby 3D printer, of an ion mobility spectrometer (IMS) with relatively high efficiency, and resolution comparable to that of commercial IMS instruments. This system uniquely operates without pneumatic forces at atmospheric pressure. The methods that Baird uses could easily become standard for applications of IMS, the most common of which is airport security screening. This example serves as a reminder that the conception and design of novel instrumentation represents science at its best intellectually as well as having a great practical value.

West Lafayette, USA
November 2016

Prof. R. Graham Cooks

Parts of this thesis have been published in the following journal articles:

1. Z. Baird, W.-P. Peng and R. G. Cooks, International Journal of Mass Spectrometry, 2012, **330–332**, 277–284.
2. Z. Baird, P. Wei and R. G. Cooks, Analyst, 2015, **140**, 696–700.

Acknowledgements

First and foremost, I would like to thank my family for their unending support and love throughout my entire life. My mother's optimism and encouragement is a constant source of inspiration and I strive to embrace these traits. Since I was young my father Gary has taught me the value of hard work, persistence, and ingenuity. My sisters Tess and Tawni inspire me to be the best person I can. I hope to live by the examples they set.

Jonny, Cherish, and Buddha have been ever-dependable and never fail to make me laugh. Thanks to Dr. Joel Rindelaub, Dr. Steve Oulette, Dr. Brett Noel, and Patrick Freeland for ensuring life wasn't taken too seriously in Lafayette. In addition, I would like to thank Eric Lien for the contribution of his seemingly unlimited knowledge and know-how in the operation and construction of 3D printers.

I'm thankful to my advisor, Dr. R. Graham Cooks for providing me with the opportunity to complete my doctoral studies in his labs. His guidance has allowed me to develop innumerable skills and expanded my knowledge in ways that would not have been possible otherwise. I also thank Dr. Zheng Ouyang for his direction and criticisms that encouraged me to develop a better understanding of my work.

I thank Dr. Jonell Samberson, Dr. Josh Wiley, Dr. Santosh Soparawalla, Dr. Jobin Cyriac, Dr. Ryan Espy, Dr. Paul Hendricks, Dr. Jon Dagleish, and Dr. Dahlia Campbell for your initial help and training in Aston Labs. I especially thank Jason Duncan and Dr. Wen-Ping Peng for all of their help with electronics and instrumentation and helping me establish a foundation in these areas. The work done by Dr. Abraham Badu-Tawiah and Dr. Anyin Li contributed greatly to my own work and I thank them for all of their guidance and contributions throughout my studies. I thank Dr. Sandilya Garimella and Michael Wleklinski for their critical insight, especially relating to simulations and data analysis. I owe thanks to all other past and present members of Aston Labs that I have had the opportunity to work with and learn from—Dr. Jacob Shelley, Alan Jarmusch, Dr. Kevin Kerian, Adam Hollerbach, Steve Ayrton, Christopher Pulliam, Dr. Fred Jjunju, Ryan Bain, Dalton Snyder, Pu Wei, Xin Yan, and Karen Yanell.

I would also like to thank the Simpson Lab, especially Dr. Scott Toth, Dr. Emma DeWalt, Paul Schmidt, Justin Newman, and Dr. Shane Sullivan, for letting me trouble them with questions about SONICC and for the use of their instruments and time. Many thanks to Dr. Garth Simpson for his help with any question I might have, the lively debates on the merits of Mathcad, and for serving on my defense committee.

Many thanks to the Purdue Chemistry Maintenance Shop, especially Betty Dexter, Ned Gangwer, and Aaron Harkleroad for their help with any and all of my requests from renting vans to bending sheet metal. Likewise, thanks to Randy Repogle for all of his help with machining parts and helping me to produce working prototypes.

I also thank Dr. Amy Davidson for serving on my committee until her passing. Thank you to Dr. Dor Ben-Amotz for agreeing to serve in her place. Thanks as well to Dr. Steve Wereley for helping me develop a better understanding of basic fluid flow and for serving on my defense committee.

Contents

List of Figures

Chapter 1
Introduction

1.1 Overview

The control and analysis of ions is most commonly performed under vacuum. The physics of ion motion under these pressures is well understood, thus ions may be identified based on their mass-to-charge ratio (m/z) through different mass spectrometry (MS) methods. The discoveries of both the electron by Thomson [1], and of isotopes by Aston [2] were made possible through the manipulation of charged particles by electric and magnetic fields under low pressure conditions. Thomson and Aston would later earn Nobel prizes for their discoveries in Physics and Chemistry, respectively, highlighting the importance of these early studies.

Gas-phase ions have several distinctive properties that are often exploited in analytical and preparative methods. Their charged nature allows them to be precisely manipulated by electric and magnetic fields for control of spatial distribution, kinetic energy, and separated for identification as a result of mass and charge differences. Additionally, gas-phase ions have exceptional reactivity as a result of their charge. Reactions of ions with neutral molecules in the gas phase is unique in that there exists a long range potential interaction and the polarization of the neutral allows for long interaction times for the ion-molecule pair [3]. This effect is exploited for the characterization of ions through reactions that are specific to functional groups present on ions of interest [4], conformational analysis of proteins and peptides [5], and to gain a better understanding of the mechanisms occurring in organic reactions [6].

Aside from its analytical uses, the separation of ions in the gas phase has a long history as a method of purification. The initial case of such a use was the purification of U^{235} for the first atomic bomb, in which large Calutron mass spectrometers employed magnetic fields to spatial resolve and collect ionized U^{235} from mixtures containing mostly U^{238} [7]. Years later, the same principle of MS purification would be applied to organic molecules in the form of ion soft landing (SL). In these experiments, ions are generally generated outside of the vacuum and

Z. Baird, *Manipulation and Characterization of Electrosprayed Ions Under Ambient Conditions*, Springer Theses, DOI 10.1007/978-3-319-49869-0_1

transferred into a MS for separation. The separated ions are then deposited on surfaces at low kinetic energies (1–100 eV) within the confines of the vacuum system [8]. SL has since been demonstrated for the preparation of protein and peptide microarrays with retained biological activity [9, 10], surface modification through reactive SL [11, 12], and the deposition of monodisperse clusters [13]. Although MS as a preparative methodology has immense benefits due to the selectivity possible, its wide use in the purification of organic molecules has not been adopted. This is mainly the result of inefficient ion production, ion losses, and low material recovery. Namely, ion transfer from an atmospheric pressure ion source into a vacuum system is associated with immense ion losses. Additionally, at higher ion beam densities space-charge has deleterious effects on the resolution of separation as well as causing additional ion loss within the vacuum system.

The work presented in this dissertation is focused on the development different methods and instrumentation designed specifically to control ions in the ambient environment, without the constraints of a vacuum system and to limit associated ion losses involved with their transfer into a low pressure analysis region. Ion motion in air at atmospheric pressure is inherently more complex than under vacuum and experiments were designed to gain a better understanding of the manners in which ions may be controlled under ambient conditions. A combined approach of simulations and experiments is used to address the topics of transfer efficiency, focusing, and analysis of ions produced by electrospray methods.

1.2 Electrospray Ionization

1.2.1 A Brief History

The observation of liquid atomization and deformation in the presence of a strong electric field dates back several centuries, the underlying theory of which was first described by Lord Rayleigh as early as 1882 [14]. It would be more than 30 years before work was undertaken by John Zeleny to gain a better understanding of this phenomenon and take the first photographs of different "modes" of electrospray from small cylindrical emitters [15, 16]. Nearly 40 years after Zeleny's observations, Sir. Geoffrey Ingram Taylor developed a theoretical model of the shape a deformed liquid meniscus assumes at the end of a capillary in the presence of an electric field, now known as a "Taylor cone" [17]. These studies laid the foundation for electrospray ionization (ESI), which would later prove to be an invaluable tool spanning many disciplines.

Around the same time Taylor was developing underlying theories of electrospray generation, Dole et al. [18, 19] showed that beams of fairly large (51–411 kDa) polystyrene ions could be generated by sampling an electrosprayed solution into vacuum. While not able to measure m/z of the ions directly, with a thorough understanding of ion-neutral interaction forces and by adjusting the potential of a

charged repeller grid, they were able to verify the formation of a beam of "macroions" rather than low molecular-weight species [18], a fact confirmed by later experiments for the analysis of electrophoretic mobilities of the electrosprayed solutions [20].

Electrospray as a tool for mass spectral analysis was driven to the forefront of analytical science through seminal work published by Fenn et al. [21, 22] in laboratories at Yale University and later Virginia Commonwealth University. His, and the subsequent work of others demonstrated the ability of ESI to produce gas-phase ions with virtually no fragmentation, even for large biologically relevant species such as proteins and oligonucleotides [23], thus making them amenable to characterization by MS. From these footings, ESI coupled with MS (ESI-MS) became a standard tool for characterization of molecules and mixtures that required "gentle" ionization.

Initially ESI emitters used by Dole and Fenn were stainless steel hypodermic needles with either a tapered or beveled tip [18, 21]. Typically the diameter of these tips was 100−200 μm with solution flow rates in the range of 1–15 μL/min and electrospray potentials of up to 2–5 kV. Later, Mann et al. [24] would demonstrate the benefits of using an emitter formed by pulling a glass capillary to a tapered tip with a diameter of about 1 μm. This design allowed for the use of lower volumes (several μL), operation without a syringe pump, as well as no sheath or drying gas for coupling with MS. The move to smaller emitters also improved detection efficiency by a factor of 510, a property largely attributed to the low flow rate (< 50 nL/min) and initial droplet size of what would come to be known as nanoelectrospray ionization (nanoESI) [25].

1.2.2 Electrospray Ion Formation

There are two prevailing theories on the mechanism by which gas-phase ions are formed from electrosprayed solutions [26]. Each of these explanations has evidence to suggest that they contribute to ion formation under certain conditions and with different types of analytes [27]. The first proposed mechanism, provided by Dole et al. [18, 24], would become known as the charged residue model (CRM). Ion formation in CRM is hypothesized to be the results of the evaporation of solvent from charged droplets to reach the Rayleigh instability limit, at which time droplets undergo columbic separation to produce smaller droplets below the Rayleigh limit. Through a cascade of these events there will eventually remain a single charged molecule, so long as the solution is sufficiently dilute. Another possibility is the so called ion evaporation model (IEM) originally proposed by Iribarne and Thomson [28]. During initial stages of charged droplet evaporation, IEM predicts the same Coulombic fission into smaller droplets, but differs in the final process. Unlike CRM, IEM predicts that upon reaching a certain radius, electric field strength on the droplet surface will reach a sufficient magnitude to expel an ion from the solvated environment of the droplet. Both IEM and CRM have an

abundance of evidence to suggest that they contribute to final formation of ions from charged droplets produced by electrospray [29].

The work done towards understanding the mechanism by which ions are formed in ESI has also led to important observations on the effects of solution properties on the identity and form of ions produced. This is perhaps most relevant for molecules such as proteins and peptides as many experiments suggest that their gas-phase conformations are highly dependent on those in solution [30–32].

1.2.3 Preparative Electrospray

Electrospray is not limited to applications involving chemical analysis, but is in fact used in a preparative sense quite frequently. The small size of droplets produced by electrospray makes them ideal for the production of micro- and nanoparticles from solutions. Particle formation is accomplished through solvent evaporation from electrosprayed droplets, which are subjected to charge neutralization (by interaction with a plasma) to prevent Coulombic fission events, and thus the formation of much smaller droplets. In cases where uniform particle size is desired, an AC frequency may be superimposed on the DC voltage applied to the emitter, creating controlled breakup of droplets of uniform size [33]. Thin films can also be readily produced by electrospray deposition (ESD) onto surfaces [34]. ESD for thin film production is advantageous in that droplets do not coalesce and are efficiently deposited on the target surface, factors governed by the highly charged nature of the droplets [35].

In recent years, electrospray has also been demonstrated as a means of performing chemical reactions at accelerated rates, relative to their solution-phase counterparts. The acceleration is likely due to several effects in evaporating microdroplets including a rapid concentration increase, an increase in relative surface area, and the large changes in pH [36, 37]. This effect occurring in electrosprayed droplets has been demonstrated through online derivatization of ketosteroids for analysis by desorption electrospray ionization (DESI) [36], a base-catalyzed Claisen-Schmidt condensation [38], the cross-linking of peptides [39], and in the Hantzsch synthesis of 1,4-dihydropyridines [40]. The accelerated reaction rates occurring in small droplets and upon the impact of electrosprayed droplets with surfaces provides a unique method of exploring reactions with small quantities of reagents and solvent that is easily coupled with MS for analysis of reaction products.

In addition to organic synthesis, nanoESI has been used to synthesize metallic nanoparticles (NPs) on surfaces. In these experiments, a wire composed of the metal of interest is used to apply a high potential to a solution of acetonitrile (ACN) in a nanospray emitter. Metal ions are generated in solution by electrolysis of the wire, and are carried by the resulting charged droplets to a grounded surface. At the surface, the metal ions are reduced and aggregate to form NPs. Particle size is dictated by the number of ions deposited, a function of both electrospray current and time. NPs generated by this method have been used as catalysts for organic

reactions as well as Raman active substrates for surface enhanced Raman spectroscopy (SERS) [41, 42]. Because the particle size is easily controlled, SERS active substrates can be tuned for different excitation wavelengths. Moreover, ions can be directed to distinct regions through the use of atmospheric pressure ion optics and electrostatic masks.

1.3 Simulations of Ion Motion at Atmospheric Pressure

The simulation of gaseous ion trajectories has been used extensively in the development of ion optics for mass spectrometry (MS), ion mobility spectrometry (IMS), electron microscopes (EM), and focused ion beam (FIB) systems. In the case of systems operating in high-vacuum (EM and FIB) the simulation environment is often simplified and assumed to be collision-free and ion motion is influenced purely by electric and magnetic fields; however, IMS and many MS systems operate in a pressure regime in which collisions must be taken into account to accurately predict ion motion [43]. The primary simulation tool used in this work, SIMION 8.0 includes two collision models: a hard sphere collision model (HS1) and a statistical diffusion simulation model (SDS). Either can be incorporated into a simulation environment for the treatment of collisions between ions and a background gas. HS1 employs hard-sphere collision kinetics to compute the resulting ion trajectory change for ion-molecule collisions individually [44]. This approach is not computationally feasible at atmospheric pressures as the mean free path in air at 25 °C is approximately 67 nm [45]. Rather than treating individual collisions, the SDS algorithm uses a combined approach of diffusion and ion mobility to simulate ion motion in electric fields.

The motion of ions at atmospheric pressure is heavily influenced by the diffusion of ions in the medium, as well as by external forces exerted on the ions (electric fields, bulk gas flow, etc.). Diffusion can be expressed as:

$$J = D\nabla_n \tag{1.1}$$

where J, D, and ∇_n are the number of ions passing through an area normal to the gas flow, a proportionality constant, and the concentration gradient, respectively [46]. In the SIMION-SDS algorithm, diffusion is simulated by imposing a jump onto the ion trajectory. The direction of the jump is randomized and it's magnitude is determined by an interpolation between collision statistics tables (selected based on the mass ratio of the ion to a background gas molecule) and scaled appropriately based on an expected number of collisions in the simulation time step [47].

When subjected to an electric field (E), the velocity of an ion in a gas with no bulk flow is determined by its mobility (K) in the buffer gas [46]:

$$v = KE \tag{1.2}$$

K is determined experimentally and is directly proportional to D and the charge (e) on the ion and inversely proportional to temperature (T) multiplied by the Boltzmann constant (k) [46]:

$$K = \frac{eD}{kT} \tag{1.3}$$

Equation 1.3 is known as the Nernst-Townsend relation and holds for the cases in which ions are thermalized. The mobility can further be expressed as [48]:

$$K = \frac{3e}{16N}\left(\frac{2\pi}{\mu kT}\right)^{1/2}\left(\frac{1}{Q_D}\right) \tag{1.4}$$

where N is the density of the neutral molecules, μ is the reduced mass of the collision pair, and Q_D is the collisional cross section (CCS). Due to the range of working conditions used in IMS instruments, the mobility of an ion is often reported as the reduced mobility (K_0) which is corrected for 273 K and a pressure (P) of 760 Torr:

$$K_0 = K\left(\frac{273}{T}\right)\left(\frac{P}{760}\right) \tag{1.5}$$

At each time step within a SIMION-SDS simulation, the velocity of an ion is subjected to the effects of gas flow and the applied electric field, in the form of ion mobility (Eq. 1.2). A simulated diffusion in the form of a random jump is superimposed on this motion to determine the location of the ion during the start of the next time-step. A detailed description of the SDS algorithm is given by Appelhans et al. [47] and in the SIMION 8.0 documentation. The SDS algorithm is capable of either using a defined mobility for each ion, or in the cases in which this data is not available, known information (particle diameters, masses, etc.) is used to estimate a value for ion mobility. Spatial variations in gas flow, pressure, and temperature may also be incorporated into the SDS algorithm to more accurately model conditions in which these parameters are known. Effects due to space charge can also be included in the modeling; however, ions must be flown as a group when incorporating space charge effects into an SDS simulation.

The implementation of the SDS algorithm into the SIMION workspace has been shown to be an accurate predictor for ion motion at or near atmospheric pressure and has been validated experimentally in several cases including traditional drift cell ion mobility spectrometry (IMS) and high field asymmetric waveform ion mobility spectrometry (FAIMS) [49–51].

1.4 Fused Deposition Modeling

Fused deposition modeling (FDM) is a 3D printing process by which a molten plastic is extruded through a heated nozzle to form an object one layer at a time [52]. While there exist a number of different 3D printing technologies, FDM is relatively inexpensive and there are a wide array of machines and materials available to consumers. Generally, a thermoplastic filament is fed to a moving print head by a drive gear at well-defined rates for the manufacture of an object on the print bed. Common materials used in FDM include poly (acrylonitrile butadiene styrene) (ABS), polylactic acid (PLA), polyamide (nylon), polyethylene terephthalate (PET), polycarbonate (PC), etc. The plastic filament must have a well-defined diameter (generally ± 0.05 mm) in order to produce an object with good precision.

The general scheme for producing an object by FDM involves four parts: (1) computer modeling of the object, (2) conversion of the model to appropriate format, (3) generation of machine tool paths, and (4) transfer of tool paths to the machine for object production. The object can be modeled in any of a number of computer aided drafting (CAD) programs depending on their availability. For the work presented herein all objects were initially modeled in Autodesk Inventor (Autodesk, CA, USA). The 3D model is then converted to a file type that represents the surfaces of the object with polygons, typically this is accomplished by exporting the part to a suitable file format. The most common file type being stereolithography file format (.stl). The.stl file is then processed using a "slicing" software which divides the object into layers and generates tool paths, most often in the form of G-Code. Within the slicing engine, several parameters can be set, including infill percentages, extrusion width, speed, and layer height. Objects manufactured by FDM are very seldom fully filled with material, but rather a sparse infill and solid perimeters. This lessens total material consumption and printing time, as well as minimizes errors caused by diameter variation in the filament. The layer height determines the resolution of the final printed object in the Z-direction, that is, the axis orthogonal to the layers produced. After the slicer has been run, the G-Code commands are sent serially to the control electronics of the printer. From these commands, the printer generates a 3D object one layer at a time.

References

1. E.A. Davis, Philos. Mag. Lett. **87**, 293–301 (2007)
2. F.W. Aston, *Mass spectra and isotopes* (Green & Co, New York, London, 1942)
3. G. Gioumousis, D.P. Stevenson, J. Chem. Phys. **29**, 294–299 (1958)
4. M. Fu, R.J. Eismin, P. Duan, S. Li, H.I. Kenttämaa, Int. J. Mass Spectrom. **282**, 77–84 (2009)
5. M.K. Green, C.B. Lebrilla, Mass Spectrom. Rev. **16**, 53–71 (1997)
6. S. Gronert, Chem. Rev. **101**, 329–360 (2001)
7. W.E. Parkins, Phys. Today **58**, 45–51 (2005)

8. B. Gologan, J.R. Green, J. Alvarez, J. Laskin, R. Graham, Cooks. PCCP **7**, 1490–1500 (2005)
9. Z. Ouyang, Z. Takáts, T.A. Blake, B. Gologan, A.J. Guymon, J.M. Wiseman, J.C. Oliver, V.J. Davisson, R.G. Cooks, Science **301**, 1351–1354 (2003)
10. B. Gologan, Z. Takáts, J. Alvarez, J. Wiseman, N. Talaty, Z. Ouyang, R.G. Cooks, J. Am. Soc. Mass Spectrom. **15**, 1874–1884 (2004)
11. M. Volný, W.T. Elam, A. Branca, B.D. Ratner, F. Tureček, Anal. Chem. **77**, 4890–4896 (2005)
12. V. Franchetti, B.H. Solka, W.E. Baitinger, J.W. Amy, R.G. Cooks, Int. J. Mass Spectrom. Ion Phys. **23**, 29–35 (1977)
13. G.E. Johnson, C. Wang, T. Priest, J. Laskin, Anal. Chem. **83**, 8069–8072 (2011)
14. L. Rayleigh, Philos. Mag. Series **5**(14), 184–186 (1882)
15. J. Zeleny, Phys. Rev. **3**, 69–91 (1914)
16. J. Zeleny, Phys. Rev. **10**, 1–6 (1917)
17. G. Taylor, Proceedings of the Royal Society of London Series A. Math. Phys. Sci. **280**, 383–397 (1964)
18. M. Dole, L.L. Mack, R.L. Hines, R.C. Mobley, L.D. Ferguson, M.B. Alice, J. Chem. Phys. **49**, 2240–2249 (1968)
19. L.L. Mack, P. Kralik, A. Rheude, M. Dole, J. Chem. Phys. **52**, 4977–4986 (1970)
20. J. Gieniec, L.L. Mack, K. Nakamae, C. Gupta, V. Kumar, M. Dole, Biol. Mass Spectrom. **11**, 259–268 (1984)
21. M. Yamashita, J.B. Fenn, J. Phys. Chem. **88**, 4451–4459 (1984)
22. J.B. Fenn, M. Mann, C.K. Meng, S.F. Wong, C.M. Whitehouse, Science **246**, 64–71 (1989)
23. T.R. Covey, R.F. Bonner, B.I. Shushan, J. Henion, R.K. Boyd, Rapid Commun. Mass Spectrom. **2**, 249–256 (1988)
24. M.S. Wilm, M. Mann, Int. J. Mass Spectrom. Ion Processes **136**, 167–180 (1994)
25. M. Wilm, M. Mann, Anal. Chem. **68**, 1–8 (1996)
26. N.B. Cech, C.G. Enke, Mass Spectrom. Rev. **20**, 362–387 (2001)
27. P. Kebarle, L. Tang, Anal. Chem. **65**, 972A–986A (1993)
28. B.A. Thomson, J.V. Iribarne, J. Chem. Phys. **71**, 4451–4463 (1979)
29. P. Kebarle, M. Peschke, Anal. Chim. Acta **406**, 11–35 (2000)
30. D.S. Gross, P.D. Schnier, S.E. Rodriguez-Cruz, C.K. Fagerquist, E.R. Williams, Proc. Natl. Acad. Sci. **93**, 3143–3148 (1996)
31. S.K. Chowdhury, V. Katta, B.T. Chait, J. Am. Chem. Soc. **112**, 9012–9013 (1990)
32. J. Loo, Mass Spectrom. Rev. **16**, 1–23 (1997)
33. W. Balachandran, W. Machowski, C.N. Ahmad, Industry Applications. IEEE Transactions on **30**, 850–855 (1994)
34. A. Jaworek, J. Mater. Sci. **42**, 266–297 (2007)
35. A. Jaworek, Powder Technol. **176**, 18–35 (2007)
36. M. Girod, E. Moyano, D.I. Campbell, R.G. Cooks, Chem. Sci. **2**, 501–510 (2011)
37. A. Badu-Tawiah, D. Campbell, R.G. Cooks, J. Am. Soc. Mass Spectrom. **23**, 1077–1084 (2012)
38. T. Müller, A. Badu-Tawiah, R.G. Cooks, Angew. Chem. Int. Ed. **51**, 11832–11835 (2012)
39. A.K. Badu-Tawiah, A. Li, F.P.M. Jjunju, R.G. Cooks, Angew. Chem. **124**, 9551–9555 (2012)
40. R.M. Bain, C.J. Pulliam, R.G. Cooks, Chem. Sci. **6**, 397–401 (2015)
41. A. Li, Q. Luo, S.-J. Park, R.G. Cooks, Angew. Chem. Int. Ed. **53**, 3147–3150 (2014)
42. A. Li, Z. Baird, S. Bag, D. Sarkar, A. Prabhath, T. Pradeep, R.G. Cooks, Angew. Chem. Int. Ed. **53**, 12528–12531 (2014)
43. R.K. Julian, M. Nappi, C. Weil, R.G. Cooks, J. Am. Soc. Mass Spectrom. **6**, 57–70 (1995)
44. D. Manura, & D. Dahl, SIMION (R) 8.0 user manual, scientific instrument services. *Inc., Ringoes, NJ*, *8551* (2008)
45. S.G. Jennings, J. Aerosol Sci. **19**, 159–166 (1988)
46. G.A. Eiceman, Z. Karpas, H.H. Hill, *Ion Mobility Spectrometry*, 3rd edn. (Taylor and Francis, Hoboken, 2013)
47. A.D. Appelhans, D.A. Dahl, Int. J. Mass Spectrom. **244**, 1–14 (2005)

48. E. A. Mason and E. W. McDaniel, in *Transport Properties of Ions in Gases*, (Wiley-VCH Verlag GmbH & Co. KGaA, Editon edn, 2005), pp. 137–193
49. H. Lai, T.R. McJunkin, C.J. Miller, J.R. Scott, J.R. Almirall, Int. J. Mass Spectrom. **276**, 1–8 (2008)
50. S. Prasad, K. Tang, D. Manura, D. Papanastasiou, R.D. Smith, Anal. Chem. **81**, 8749–8757 (2009)
51. W. Wissdorf, L. Pohler, S. Klee, D. Müller, T. Benter, J. Am. Soc. Mass Spectrom. **23**, 397–406 (2012)
52. I. Gibson, D.W. Rosen, B. Stucker, *Additive manufacturing technologies*, vol. 238 (Springer, New York, 2010)

Chapter 2
Ion Transport and Focal Properties of an Ellipsoidal Electrode Operated at Atmospheric Pressure

2.1 Introduction

Most frequently, ions are transported from ambient pressure and manipulated under low pressure conditions. While a vacuum environment is necessary to make precise measurements of an ion's mass-to charge ratio, the ability to effectively control ion trajectories and spatially manipulate ions without the use of vacuum systems is of great interest in a number of different fields. Modifications to surfaces made using low energy molecular ion beams [1–9] are of particular note. Such modifications include cases in which the ion/surface interaction occurs at atmospheric pressure [10, 11]. Applications include the chemical functionalization (derivatization) of surfaces [12, 13] and the preparation of thin films [14, 15]. While thin film preparation typically uses exposure to highly controlled yet poorly characterized plasmas [16], polymer film deposition using ion beam conditioning has become increasingly common [17]. Ambient ionization, particularly in the field of analytical mass spectrometry relies on the ionization and subsequent transfer of ions to a vacuum system for analysis. This field focuses on the analysis of samples via mass spectrometry in their native state, with little-to-no sample preparation. A wide variety of ambient ionization methods have been developed and include spray, laser, and plasma techniques which are used to generate representative ions [18, 19]. The growth of interest in gas-phase ion chemistry under ambient environment raises obvious concerns regarding ion transport and focusing at atmospheric pressure. An understanding of factors which contribute to the efficiency by which ions are transported has come both empirically (e.g. the transport over several meters of ions generated by desorption electrospray ionization, and their delivery to a mass analyzer [20]) as well as through fluid dynamics simulations [21]. These simulations have confirmed that once laminar flow is established in a transport tube, modest suction will move typical organic ions long distances through air without significant losses.

Z. Baird, *Manipulation and Characterization of Electrosprayed Ions Under Ambient Conditions*, Springer Theses, DOI 10.1007/978-3-319-49869-0_2

The issue of ion focusing in air is has importance beyond the ambient ionization methods. In particular, all forms of spray ionization, including electrospray ionization (ESI), yield droplets, the fission of which results in a highly dispersed spray plume in which the ion concentration decreases rapidly with distance from the source [22]. This undesirable effect is compounded by the fact that the droplets undergo further fission and desolvation before producing gas-phase ions that can be analyzed by a mass spectrometer. Increased distances of travel are needed for more effective desolvation [23, 24]. On the other hand, the small sampling orifices (generally 1 mm or less, inner diameter) needed for vacuum compatibility greatly restrict the fraction of ions that may be sampled from the spray plume. Because of these factors, ion collection efficiency is low, typically a small fraction of the ions produced (often <0.1 %) by the ionization source [22, 25].

Multipole ion guides based on collisional focusing through the application of radio frequency (RF) fields have been utilized to increase transport efficiency at lower pressures (0.1–10 mtorr) but the same effect is not observed at atmospheric pressure [26, 27]. Another popular approach is through the use of electrodynamic ion funnels. Ion funnels are composed of stacked ring electrodes of decreasing diameter to which DC and RF potentials are applied. In some cases these have improved sensitivity by more than 10 fold when operated in the first differentially pumped regions of a mass spectrometer. However, the ion funnel is only effective in the pressure range of 0.1–30 torr and is a mechanically complex device [28]. Other methods utilizing stacked ring electrodes have also been demonstrated as a means of increasing ion transmission; however their function is limited to intermediate pressures (ca. 1 mtorr—1 torr). Such methods include the traveling wave ion guide which uses electrodynamic potentials to confine ions radially along with a superimposed voltage pulse to transport ions axially, and the periodic focusing ion guide, which uses only DC potentials to provide periodic ion focusing [29, 30]. As the majority of ion loss takes place at the atmospheric pressure interface of a mass spectrometer, improvement in transport from ambient pressure to the first differentially pumped region is needed to improve sensitivity significantly.

Herein is described the use of a simple elliptical electrode to which only DC potentials are applied to facilitate the efficient transport and focusing of ions at atmospheric pressure. An ellipsoidal shape was chosen to be compatible with the intended future use of an array of spray tips as a means of increasing ion currents. The ellipsoidal shape provides symmetry in the sprayer orientation as each sprayer can be angled to spray towards the same point while experiencing equivalent potentials imposed by the focusing electrode structure. Interest is concentrated on ions produced by ion sources which have low solvent flow rates, typified by nanoESI. The focal properties of the electrode system is explored through the use of a detector that operates at ambient pressure. Quantitative measurements of ion transfer efficiency are made using ionized dyes which, after soft landing onto a surface, can be rinsed off and quantified spectrophotometrically. When interfaced to the atmospheric pressure inlet of a mass spectrometer, the ion optical system described here is shown to increase ion transport efficiency by a factor of 100 over distances of several centimeters.

2.2 Experimental

2.2.1 Chemicals and Instrumentation

All mass spectra shown herein were taken on a Thermo LTQ linear ion trap mass spectrometer (Thermo Scientific, San Jose, CA, USA) over a mass range of *m/z* 100–2000. Prior to use, the instrument was calibrated according to procedures outlined in the LTQ user manual. Solutions for positive ion calibration were prepared in-house and consisted of a mixture of caffeine, a short chain peptide salt (Met-Arg-Phe-Ala acetate, MRFA), and Ultramark 1621. For negative spectra sodium dodecyl sulfate and sodium taurocholate was included in the positive ion mixture. These solutions were prepared according to instructions provided in the user manual. Detection of the spatial distribution of ions at atmospheric pressure was accomplished through the use of an IonCCD™ detector system (OI Analytical, Pelham, AL, USA) with an integration time of 100 ms. Experiments in which the transport efficiency of ions was tested utilized a 1 mM solution of rhodamine B in 4:1 methanol:water (v:v). A Cary 300 UV–Visible spectrophotometer (Agilent Technologies, Santa Clara, CA, USA) was used for the collection of absorption spectra. Chemicals and solvents were purchased from Sigma-Aldrich (St. Louis, MO, USA).

2.2.2 Ion Transport and Beam Profiling

The assembly used to demonstrate the transmission and focusing of ions beams at atmospheric pressure in the experiments discussed within this chapter is shown in Fig. 2.1 as a cutaway view with relevant axes identified. It was manufactured from a solid stainless steel block which was milled out to form a polished, half-ellipsoidal cavity (4.3 and 1.8 cm major and minor radii, respectively). Holes were drilled on the top portion of the block, to allow for the insertion of nanoESI tips for the generation of ions, as well as a single inlet on the bottom portion through which a supplementary gas flow could be introduced. Dry nitrogen was delivered from a compressed cylinder for experiments in which a gas flow was employed. A polyether ether ketone spacer (PEEK) provided electrical isolation of the ellipsoidal electrode from grounded aluminum plate covering the opening of the cavity. For all experiments the spacing between the aluminum plate and the opening of the stainless steel electrode (z = 0) was 2 mm.

Generation, transport, and subsequent focusing of ions was accomplished by first inserting a nanoESI spray tip through one of several holes in the top of the steel electrode. Once the spray tip was inserted, the potential on the spray tip and ellipsoidal electrode were adjusted such that the difference between the two was the effective spray voltage, and the difference between the electrode and aluminum plate was the focusing potential. For example, a potential of 3 kV applied to the electrode, 4.0 kV to the sprayer, with the aluminum plate held at ground results in a

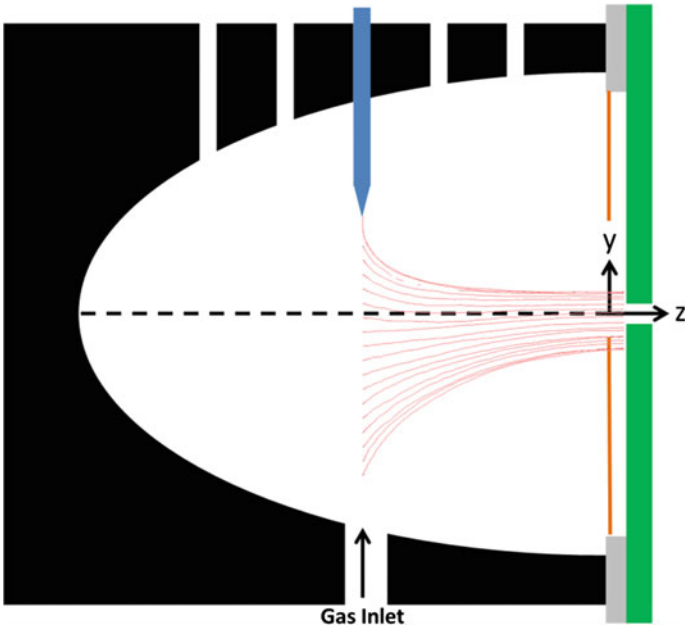

Fig. 2.1 Two dimensional representation of focusing assembly showing the stainless steel electrode (*black*), spray tip (*blue*), PEEK insulator (*gray*), and the grounded aluminum plate (*green*). Direction of axes are shown in the lower *left* with the x-axis orthogonal to the paper. The *dashed line* represents the center (z) axis of the electrode and the *orange line* is used to show the opening plane of the ellipse and is used to define z = 0. *Red traces* are plots of ion trajectories

positive-mode electrospray at a spray voltage of 1.0 kV with a focusing potential of 3.0 kV. Focusing potentials ranging from 1 to 6 kV with spray voltages in the range of 0.6–3 kV were used for all experiments described.

The full profile of the ion beam exiting the ellipse was determined by mounting the IonCCD™ with the pixel axis parallel to the y-axis and sprayer. Ion intensity profiles were taken in 0.5 mm increments across the x-axis as shown in Fig. 2.2. This experiment, including the ionization, ion transport, and detection steps was done in air without supplementary gas flow. The elliptical electrode and sprayer were held at potentials of 4 and 5 kV, respectively, while the sprayer was 25 mm from the opening plane of the ellipse (z = −25 mm). The instrument calibration mixture was used as the spray solution in all cases.

2.2.3 Ion Transport Efficiency

The efficiency of ion transport achieved with the use of the elliptical electrode assembly was explored by spraying a known amount of rhodamine B solution (1 mM)

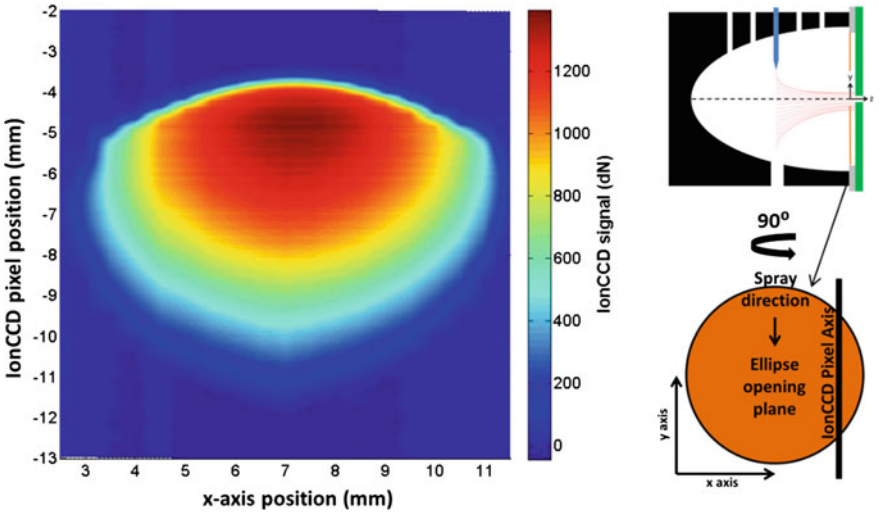

Fig. 2.2 Intensity profile of ion beam exiting ellipse in arrangement shown in Fig. 2.1, with the grounded aluminum plate replaced by an IonCCD™ detector. Potentials on ellipse and sprayer were 4 and 5 kV, respectively. Experimental setup for profiling experiment is shown in the *right* segment of figure

at different distances from the counter electrode (grounded aluminum plate) with and without the use of the elliptical electrode. The ions created were directed to and collected on the grounded aluminum plate. The material deposited on a square 1 cm^2 area corresponding to the most intense region of each deposited spot was redissolved in 1:1 methanol:water (v:v) and the solutions were analyzed for concentration by UV–Vis spectrophotometry, by employing standards of known concentration to construct a calibration curve. Quantitation was based on maximum absorbance at a wavelength of 551 nm where the molar absorptivity is 105,700 M^{-1} cm^{-1}.

2.2.4 Ion Trajectory Simulation

Several simulations were performed using the SDS algorithm to determine the trajectories of ions within the electrode and analyze the effect of varying potentials applied to each component as well as the positioning of the nanoESI tip within the electrode. The files used to generate the geometry for machining the electrode were converted to potential array (PA) files using the SL Toolkit included with SIMION 8.0. These arrays were refined using the skipped point refining method to solve for the electric field within the electrode. In each simulation the reduced mobility and diameter of each ion was estimated via the SDS algorithm. 2D images of simulated ion intensity at the deposition surface were constructed from simulation data using custom Matlab programs developed for SIMION data analysis.

2.2.5 Mass Spectrometer Interface

The electrodes were coupled to the atmospheric pressure inlet (API) of the mass spectrometer by drilling a 2.36 mm hole through the aluminum plate and inserting the 3.15 mm protrusion of the 2.28 mm outer diameter API capillary. The voltage on the capillary, as set in the LTQ software, was 15 V and electrical contact caused the potential on the aluminum plate to match this. Ions were sampled into the vacuum system of the MS through combined effects of suction at the opening of the API capillary as well as electrostatic focusing as a result of the potential applied to the focusing electrode. It is important to note that because of the relatively large area (1 cm^2) to which focused ions are directed, only a fraction of the ions impinging on the aluminum plate are sampled by the MS. LTQ calibration mix containing caffeine, MRFA peptide, and Ultramark 1621 was used as the spray solution in all experiments. The dependence of mass spectral intensity on the voltage applied to the different components was tested by scanning the potential of the ellipse from 1 to 6 kV while the sprayer was held at a constant offset of +1 kV in relation to the ellipse potential. The intensities of the protonated caffeine ion (*m/z* 195), MRFA peptide (*m/z* 524), and a peak from the Ultramark 1621 (*m/z* 1322) were recorded as a function of the potential applied to the ellipse.

2.3 Results and Discussion

2.3.1 Focusing of Electrosprayed Ions

A 2D intensity map of ions impinging on the deposition surface was constructed from intensity profiles (dN) at each position along the x-axis, shown in Fig. 2.2. Potentials applied to the sprayer and electrode were 5 and 4 kV, respectively. The resulting intensity plot indicates that the highest ion intensity occurs in the region nearest the spray tip.

Cross-sections (through center of ellipse opening plane, parallel to the y-axis of Fig. 2.2) of spatially resolved ion intensity were recorded using the IonCCD™ while the elliptical electrode was held at a constant potential of 4 kV and the sprayer was positioned 25 mm from the opening plane of the ellipse (z = −25 mm). The spray potential was varied from 4.6 to 6 kV, corresponding to offset potentials of 0.6–2 kV. While an increase in the offset potential increased the overall ion intensity, this also had the effect of broadening the profile (i.e. widening the deposition area). The broadening was likely due to the electrical fields created by the potential difference of the spray tip from the ellipse. The asymmetric nature of the ion beam was most likely the result of the orthogonal position of the sprayer relative to the center axis of the ellipse. The spray was positioned in this manner so that neutral droplets expelled from the spray tip would impinge on the electrode wall rather than be accepted into the MS. The asymmetry is not observed when the

spray direction is in-line with the center axis. The effect the offset voltage (spray potential–ellipse potential) has on both the intensity and spatial distribution of ions exiting the ellipse is shown in Fig. 2.3a.

If one considers the relationship between the maximum recorded intensity as a fraction of the total intensity (I_{max}/I_{tot}) as a function of the potential offset between the spray tip and the focusing potential it is possible to develop a method of quantifying the focal abilities of the electrode under different conditions. A plot of this is shown in Fig. 2.3b. From the plot it is clearly evident that lowering the potential offset of the spray tip from the focusing potential results in greatly increased focal abilities. Additionally, the asymmetric nature of the ion distribution is almost entirely eliminated at lower potentials compared to the distributions obtained at higher offset potentials. While a smaller number of ions are created, the

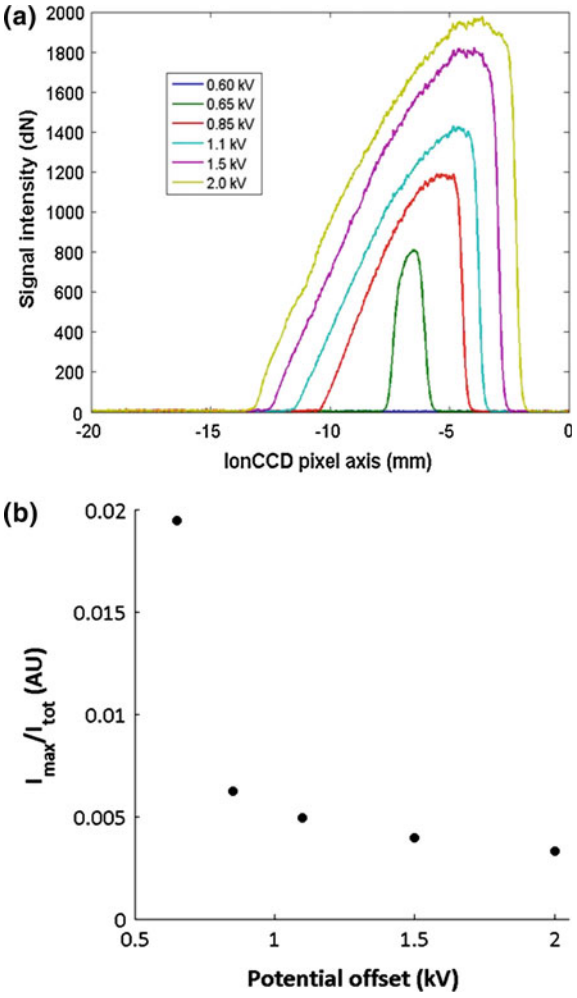

Fig. 2.3 **a** Ion intensity profile at different offset voltages and **b** maximum IonCCD™ signal (I_{max}) as a fraction of total signal (I_{tot}) for different offset potentials. Potential applied to ellipse was 4 kV and sprayer was 25 mm from the ellipse opening plane (z = −25 mm) for values shown. Spray was in the direction of decreasing values on the IonCCD™ pixel axis. The electrode arrangement corresponds to that shown in Fig. 2.1

better focusing will allow a larger percentage of ions to be sampled by a mass spectrometer, improving overall efficiency and reducing the sample volume needed for analysis. This effect is likely due to the repulsive nature of ESI plume, which is magnified at higher potentials as the density of charge increases at the spray tip.

The effect of a gas flow on the focal and transport properties of the device was examined by subjecting the ions to a nitrogen flow from a compressed gas cylinder. The pressure of the nitrogen line, as determined by the regulator, was approximately 5 psi and the interior of the device was assumed to be at atmospheric pressure. Spatial ion distributions were recorded by the IonCCD™ at different offset potentials while the ellipse potential was held constant in the same manner as described earlier. Results of these experiments show an increased intensity and an increased symmetry in the ion beam cross-section; however, the better focus at low offset potentials was not observed. This effect is likely due to the transport of ions and charged microdroplets from areas of low electric field strengths to those of higher strength where they are more highly influenced by electrostatics. Additionally, the removal of solvent vapor decreases its partial pressure within the spray plume to afford more effective solvent evaporation according to Henry's Law.

2.3.2 Simulated Ion Trajectories

A simulated map of the ion flux at the grounded deposition plate is shown in Fig. 2.4. Each of the images in the figure show the predicted effect of altering the potential applied to the spray emitter. From these results it is evident that altering this potential is likely to have a noticeable effect on the resulting ion beam shape as it exits the electrode. A range of different ion mobilities was explored via simulation, each providing the same resulting intensity plots at the grounded plate. It is important to note that these simulations do not attempt to predict the overall intensity difference under these varied conditions. The total ion current is much greater at higher emitter potentials so it is reasonably expected that the true current at the surface would in fact be much greater in Fig. 2.4c when compared with Fig. 2.4a.

While space charge plays a role in determining the trajectories of ions within the electrode, the methods of incorporating space charge included with SIMION do not effectively model the space charge interaction at ion sources. Because of this, these effects were not included in the simulations of ion motion in the elliptical electrode. Instead, ions were given an initial filled sphere distribution centered at different locations relative to the nanoESI spray tip. This method allows for a qualitative understanding of trajectories ions undergo in the elliptical electrode to aid in the improvement of electrode designs.

The simulated contour plots of ion intensity when the spray emitter is set 1 kV above that of the elliptical electrode appear to mimic the shape of the experimentally mapped ion intensity (to a limited extent) as measured with the IonCCD™ detector. As the spray potential is raised (in relation to the focusing potential), this

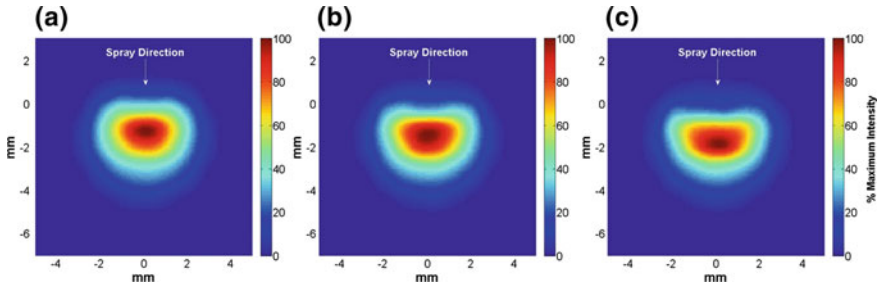

Fig. 2.4 Contour plots of simulated ion intensity at the ground plate of the ellipse for sprayer potentials of **a** 6, **b** 6.5, and **c** 7 kV. Ellipse potential was 5 kV in all cases. Ions were given a filled-sphere initial distribution with radius of 1 cm, centered 0.5 cm below the axis of the ellipse, directly below the spray tip (25 mm from opening plane of ellipse). (0, 0) coordinate corresponds to the center of ellipse opening plane

correlation no longer holds, yet the experimentally observed result of a broadened ion beam is apparent. One likely reason for this disagreement between experiment and simulation is that the phenomenon of charged droplet trajectories from a spray tip is not well modeled with the SIMION-SDS model. The effects of droplet evaporation, droplet breakup, and the differing velocities of droplets ejected from the tip in the range of potentials studied are not considered. The use of the SIMION-SDS algorithm did however, allow for a qualitative study and understanding of ion behavior inside the elliptical electrode.

2.3.3 Ion Transport Efficiency

The overall efficiency of ionization by nanoESI and ion/charged droplet transport to a collector surface was measured with and without using the elliptical focusing electrode through the deposition of the dye rhodamine B. The sprayer was 17 mm from the grounded aluminum collection plate (15 mm from the opening plane of the ellipse) in both experiments while voltages of 4 and 5.5 kV were applied to the ellipse and sprayer (1.5 kV difference) in the experiment with the focusing electrode and a spray potential of 1.5 kV was used without the ellipsoidal lens. Rhodamine B was diluted in 4:1 methanol:water (60 μL, 1 mM) and sprayed at a grounded aluminum plate. Following the deposition, the resulting material on a 1 cm^2 area on the grounded aluminum collection surface, (centered on the deposition area), was redissolved in 1:1 methanol:water (v:v), diluted to a known volume and analyzed for concentration by UV–Vis spectrophotometry. Around 15 % of the rhodamine B in the spray solution was deposited in the 1 cm^2 collection area using nanoESI without the elliptical electrode. With the elliptical electrode and using the same sprayer to counter electrode distance, the entire visible spot was confined within the 1 cm^2 collection area. Measurement of the concentration of the

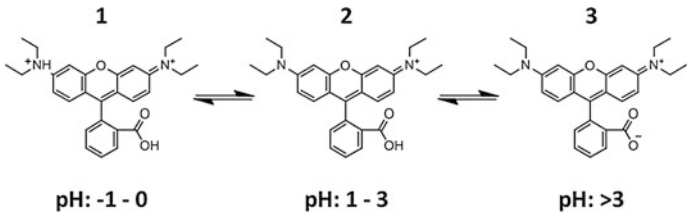

Scheme 2.1 Rhodamine B species in solution at low pH *1*, moderate pH *2*, and high pH *3*

dye taken up in a fixed volume of solvent showed that the contents of this spot corresponded to 70 % of the theoretical yield. These results show that the elliptical electrode is able to concentrate ions/charged droplets into the deposition area to produce a four-fold increase in ion intensity when compared to nanoESI without the use of a focusing electrode. The 1 cm^2 collection area was chosen to represent applications in ambient surface preparation techniques. It is not representative of applications in which ion transfer into a mass spectrometer from an atmospheric pressure ion source is of interest; in such cases the sprayer would be placed closer to a much smaller entrance capillary.

It should be noted that the 70 % efficiency value measured includes both ionization and transport to the collector surface and both processes individually must therefore be highly efficient. Attempts to draw distinctions between dry ion, solvated ion, and charged droplet focusing were not made, as these are all instances of charged particle focusing which was the objective of the experiment; however, it does seem to be important to determine the significance of the transport of analyte in the form of charged droplets. To make this distinction, the above deposition experiments were repeated using a rhodamine B solution doped with ammonium hydroxide, to give a pH of approximately 9 (0.148 M NH_4OH). Rhodamine B exists in three different forms which depend on the solution pH, as shown in Scheme 2.1 [31].

At low pH (−1 to 0) form 1 is favored, but in a solution of moderate pH (1–3), as is found in the spray solution absent a pH modifier, the cation 2 can be assumed. In a solution of higher pH the zwitterion (3) will be the favored form. Although droplet desolvation during drying in air will result in a lowered pH, this is assumed to contribute minor changes to the form of rhodamine B as the change is rarely more than 2 pH units [32]. Because of this it is assumed the deposition at low to moderate pH involves ionic species while at high pH the zwitterion should dominate. The deposition of the basic ammonium solution showed a deposition efficiency of 10 % when compared to theoretical yield (with the use of the elliptical electrode). These results are indicative of the large role played by solution phase ions in the conveyance of chemical species by electrospray, as the zwitterion (3) is effectively neutral, limiting transport to a mechanism associated with charged droplets and incidental neutral collisions.

2.3.4 Mass Spectrometer Interface

The transport of ions from the elliptical lens to the MS was investigated by comparing the ion signal recorded by the MS using the elliptical electrode to the intensities recorded by nanoESI without the electrode but with the same tip to inlet distance. When the elliptical electrode was used potentials of 3 and 4 kV were supplied to the ellipse and sprayer, respectively, while the spray tip was 22 mm from the MS inlet. For the study of intensities without the use of the ellipse, the sprayer was again positioned 22 mm from the inlet and was shielded from air currents that might disrupt the signal intensity. The potential applied to the sprayer in this case was 1 kV to match the offset potential used when the elliptical electrode

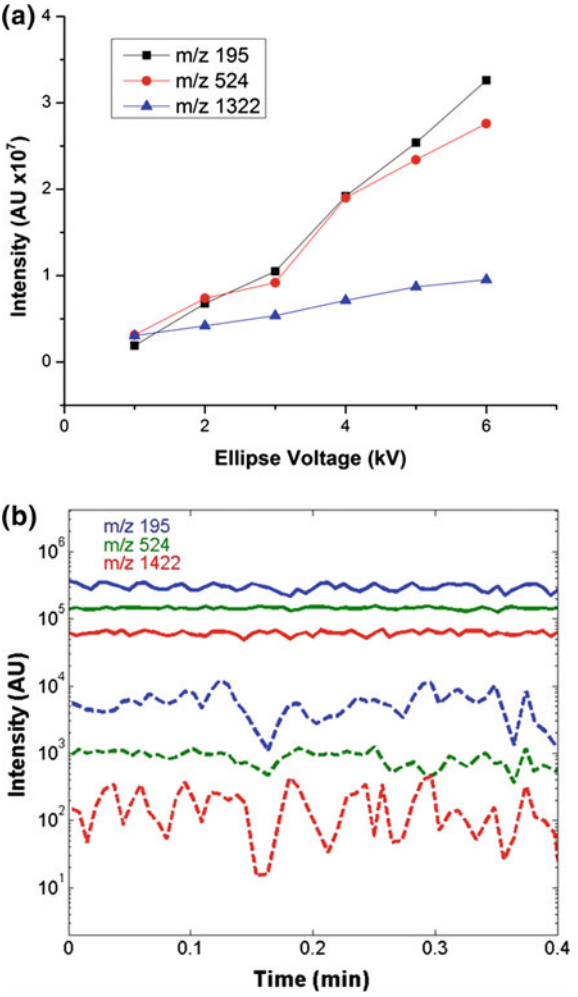

Fig. 2.5 Intensities of different ions detected by MS as a function of potential applied to elliptical electrode: **a** sprayer potential held 1 kV higher than ellipse potential throughout scan and **b** chromatograms of ion intensities using the ellipse electrode (*solid lines*) and without the ellipse electrode (*dashed lines*). Potentials of 3 and 4 kV were applied to the ellipse and sprayer, respectively. For nanoESI without the elliptical electrode, spray potential was 1 kV. In **a** the sprayer was 27 mm from the inlet of the LTQ. Tip to inlet distance for Fig. 2.6b was 22 mm

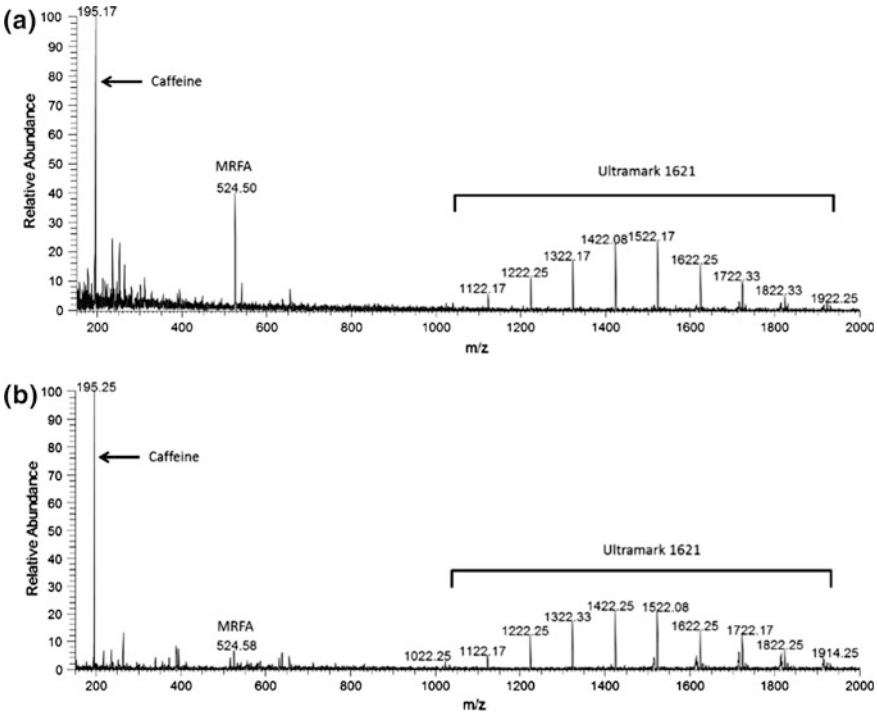

Fig. 2.6 **a** Spectrum recorded for LTQ calibration solution using the elliptical electrode with potentials of 6 and 5 kV applied to the sprayer and ellipse, respectively and **b** spectrum taken for LTQ calibration solution without the use of the focusing electrode at a spray potential of 1 kV. The spray tip to inlet distance was 22 and 3.3 mm in **a** and **b**, respectively

was employed. Figure 2.5b shows the result of these experiments by plotting a chromatogram of several ions characteristic of the calibration solution.

The results shown in Fig. 2.5a clearly indicate that increasing the potential of the electrode and sprayer results in an increased number of ions delivered to the mass spectrometer. With the larger ion (*m/z* 1322), the intensity increase is not as dramatic. As larger ions are less mobile than their smaller counterparts, they are transported to the inlet at a slower rate so that less signal is observed. The result is an increased sensitivity for smaller ions when using the elliptical electrode. Up to an 100 fold enhancement of ion signal was achieved with the use of the elliptical electrode at distances of several centimeters. It must be noted that intensities higher than those obtained with the elliptical electrode are possible through the use of nanoESI alone. This is accomplished by placing the spray tip in close proximity (2–5 mm) to the inlet; however, this does not always allow for sufficient evaporation of solvent and the spectra obtained are remarkably different in regards to relative ion intensity. Additionally, operation in this manner has the potential to introduce a large amount of contamination on the inlet of the mass spectrometer, manifested as carryover between experiments. One exemplary result of the use of the elliptical

electrode was a 4-fold increase in the signal to noise ratio for the detection of MRFA peptide (*m/z* 524) over that achieved even at optimum proximity for nanoESI without the focusing electrode (Fig. 2.6).

The congested appearance of the *m/z* 150–300 range in Fig. 2.6a also supports the conjecture of a mobility dependent ion delivery when using the ellipsoidal electrode as these ions are the same as those seen in low abundance in Fig. 2.6b. A spray distance of several centimeters is impractical for normal nanoESI analysis, but this distance allows for the inclusion of additional sprayers at different distances when the objective of the experiment is to obtain large ion currents. Such cases include ion soft landing, surface modification using ions under ambient conditions, as well as the exploration of novel chemistry observed in ambient ion-molecule reactions in which higher yields remain an issue for practical use.

2.4 Conclusions

In this study simple DC-only potentials were applied to an ellipsoidal focusing element to focus organic ions generated by nanoESI in air. The ion focusing depends on the voltage of the elliptical electrode, that of the ion source, and the distance between the source and the MS aperture. Focusing improved signal in experiments representative of two scenarios: (i) atmospheric pressure surface modification of a relatively large surface area using an ion beams and (ii) ion introduction into a mass spectrometer from a sprayer placed at a fixed and relatively large distance from the inlet. In the first type of experiment an ion transport efficiency of 70 % and a stable signal was achieved relative to ca. 15 % without focusing. In the second type of experiment the relative intensity for the peptide MRFA was four times larger at 22 mm with the focusing lens than it was at 3.3 mm without focusing. Simulations of ion motion matched experiments reasonably well in consideration of the simplified simulation environment employed.

References

1. P. Wang, J. Laskin, Angew. Chem. Int. Ed. **47**, 6678–6680 (2008)
2. D.C. Lim, R. Dietsche, M. Bubek, T. Ketterer, G. Ganteför, Y.D. Kim, Chem. Phys. Lett. **439**, 364–368 (2007)
3. S. Tepavcevic, A.T. Wroble, M. Bissen, D.J. Wallace, Y. Choi, L. Hanley, J. Phys. Chem. B **109**, 7134–7140 (2005)
4. S. Lee, L.M. Molina, M.J. López, J.A. Alonso, B. Hammer, B. Lee, S. Seifert, R.E. Winans, J. W. Elam, M.J. Pellin, S. Vajda, Angew. Chem. Int. Ed. **48**, 1467–1471 (2009)
5. H.J. Rader, A. Rouhanipour, A.M. Talarico, V. Palermo, P. Samori, K. Mullen, Nat. Mater. **5**, 276–280 (2006)
6. N. Thontasen, G. Levita, N. Malinowski, Z. Deng, S. Rauschenbach, K. Kern, J. Phys. Chem. C **114**, 17768–17772 (2010)
7. J. Cyriac, T. Pradeep, H. Kang, R. Souda, R.G. Cooks, Chem. Rev. **112**, 5356–5411 (2012)

8. K.J. Kitching, H.N. Lee, W.T. Elam, E.E. Johnston, H. MacGregor, R.J. Miller, F. Turecek, B.D. Ratner, Rev. Sci. Instrum. **74**, 4832–4839 (2003)
9. M. Volný, W.T. Elam, A. Branca, B.D. Ratner, F. Tureček, Anal. Chem. **77**, 4890–4896 (2005)
10. A. Badu-Tawiah, J. Cyriac, R. Cooks, J. Am. Soc. Mass Spectrom. **23**, 842–849 (2012)
11. A.K. Badu-Tawiah, C. Wu, R.G. Cooks, Anal. Chem. **83**, 2648–2654 (2011)
12. G.E. Johnson, Q. Hu, J. Laskin, Annu. Rev. Anal. Chem. **4**, 83–104 (2011)
13. , US20030157269A1, 2003
14. L. Hanley, S.B. Sinnott, Surf. Sci. **500**, 500–522 (2002)
15. D.R. Ifa, C. Wu, Z. Ouyang, R.G. Cooks, Analyst **135**, 669–681 (2010)
16. S. National Research Council, *Plasma Processing of Materials: Scientific Opportunities and Technological Challenges* 9780309583756 (National Academies Press, Washington, DC, USA, 1991)
17. A.T. Wroble, J. Wildeman, D.J. Asunskis, L. Hanley, Thin Solid Films **516**, 7386–7392 (2008)
18. D.J. Weston, Analyst **135**, 661–668 (2010)
19. M.-Z. Huang, C.-H. Yuan, S.-C. Cheng, Y.-T. Cho, J. Shiea, Annu. Rev. Anal. Chem. **3**, 43–65 (2010)
20. I. Cotte-Rodriguez, R.G. Cooks, Chem. Commun. 2968–2970 (2006)
21. S. Garimella, W. Xu, G. Huang, J.D. Harper, R.G. Cooks, Z. Ouyang, J. Mass Spectrom. **47**, 201–207 (2012)
22. J.S. Page, R.T. Kelly, K. Tang, R.D. Smith, J. Am. Soc. Mass Spectrom. **18**, 1582–1590 (2007)
23. J.B. Fenn, M. Mann, C.K. Meng, S.F. Wong, C.M. Whitehouse, Mass Spectrom. Rev. **9**, 37–70 (1990)
24. P. Kebarle, L. Tang, Anal. Chem. **65**, 972A–986A (1993)
25. N.B. Cech, C.G. Enke, Mass Spectrom. Rev. **20**, 362–387 (2001)
26. D. Douglas, J. French, J. Am. Soc. Mass Spectrom. **3**, 398–408 (1992)
27. A.V. Tolmachev, I.V. Chernushevich, A.F. Dodonov, K.G. Standing, Nucl. Instrum. Methods Phys. Res., Sect. B **124**, 112–119 (1997)
28. R.T. Kelly, A.V. Tolmachev, J.S. Page, K. Tang, R.D. Smith, Mass Spectrom. Rev. **29**, 294–312 (2010)
29. K. Giles, S.D. Pringle, K.R. Worthington, D. Little, J.L. Wildgoose, R.H. Bateman, Rapid Commun. Mass Spectrom. **18**, 2401–2414 (2004)
30. K.J. Gillig, B.T. Ruotolo, E.G. Stone, D.H. Russell, Int. J. Mass Spectrom. **239**, 43–49 (2004)
31. R.W. Ramette, E.B. Sandell, J. Am. Chem. Soc. **78**, 4872–4878 (1956)
32. S. Zhou, B.S. Prebyl, K.D. Cook, Anal. Chem. **74**, 4885–4888 (2002)

Chapter 3
Ion Manipulation in Air Using a System of Curved 3D Printed Plastic Electrodes

3.1 Introduction

Mass spectrometry (MS) is arguably one of the most widely used scientific tools with applications ranging from complex mixture analysis [1, 2] to molecular biology [3] and even large-scale purification and materials preparation [4, 5]. Because the fundamental basis for MS relies on a low number of collisions, the operation of a mass spectrometer requires the establishment of a low pressure environment. The first forms of mass spectrometry required that ions be produced within the vacuum system of the instrument, greatly limiting the range of compounds that could be analyzed and the throughput of analysis. This problem was largely solved with the development of atmospheric pressure interfaces (APIs), which allowed for ions to be generated at atmospheric pressure, removed from the vacuum system necessary for mass analysis. As a direct result, ambient ionization methods were born. Ambient ionization methods allowed for a sample to be directly interrogated with little-to-no sample preparation [6]. While ambient ionization provides a means of sampling, the ions produced must still undergo transfer, focusing and analysis under vacuum conditions. This is problematic as vacuum pumps are perhaps the greatest barrier to overcome in the development of miniature MS systems due to both their size and the amount of power required for their operation, which limits their practical use in a number of application areas [7].

Another method of analyzing gas-phase ions, which doesn't necessitate the use of a vacuum system is Ion mobility spectrometry (IMS). IMS is often coupled to MS platforms as a means to achieve another dimension of separation [8]. In IMS ions are separated based on their interaction with a background gas in combination with electric fields [9]. IMS instruments are typically operated at pressures much higher than that of an MS system, including atmospheric pressure; however, in order to attain acceptable resolution it is necessary to establish laminar gas flow throughout the analysis region as well as maintain a highly uniform pressure, temperature, and gas composition.

Z. Baird, *Manipulation and Characterization of Electrosprayed Ions Under Ambient Conditions*, Springer Theses, DOI 10.1007/978-3-319-49869-0_3

In their current forms, both MS and IMS share commonalities in regards to the creation of ions in the ambient environment and their subsequent transfer into an analysis region in which pressure, temperature, and humidity are well regulated. The spatial control of ions under vacuum is a mature subject and is employed in a wide range of instruments which includes MS and IMS systems as well as electron microscopes, particle accelerators, as well as a variety of surface analysis and modification methodologies [10, 11]. Yet, the control of ions at or near atmospheric pressure is much less developed, despite the rich chemistry accessible at these more manageable conditions. In recent years there have been a number of publications highlighting the unique reactivity of gaseous ions under ambient conditions and their use in the preparation of surfaces [12–15]. The manipulation and control of these ions is crucial if they are to be utilized to full potential.

The aim of this work is to perform all of the relevant tasks required for an MS or IMS system by demonstrating the generation and transfer of ions, their subsequent focusing, ion/molecule reactions in the gas-phase, separation of ions, and finally to detect ions; all performed in the ambient environment. Furthermore, all of these demonstrations are shown using plastic electrodes produced via rapid prototyping. Of which any lab equipped with a low-cost FDM 3D printer is capable of producing. In some experiments the device is used to prepare ions for subsequent analysis by a mass spectrometer while in other cases the electrodes are operated independently as a reactor/analysis system.

3.2 Experimental

3.2.1 Production and Focusing of Ions in Air

Gas phase ions are commonly produced through the use of electrospray ionization (ESI). In brief, the principle of ESI is based on the principle that upon desolvation, electrosprayed droplets produce ions of organic molecules with very little, if any fragmentation [16]. Current MS and IMS instruments rely heavily on the use of ESI as a method of producing ions from aqueous solutions, especially in the field of proteomics. In additions to these roles, ESI is the basis for a number of ambient ionization sources including: desorption electrospray ionization (DESI), laser ablation electrospray ionization (LAESI), extractive electrospray ionization (EESI), paper spray ionization (PS), etc. [6]. Perhaps one of the most profound caveats of this otherwise robust ion source is the inherent low ionization efficiency. This, in combination with the dispersive nature of an ESI plume typically results in all but a miniscule portion of generated ions lost to the surrounding environment. As a result a very small fraction of ions are available for analysis in MS experiments [17]. The overall effect is a decrease in analytical sensitivity and inefficient product collection in preparative experiments such as ion soft landing [18, 19].

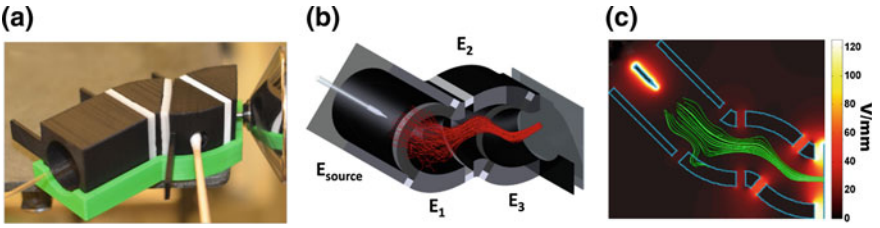

Fig. 3.1 3D printed electrode assembly interfaced with inlet of MS (**a**); cutaway rendering of assembly with overlaid ion trajectories shown in *red* (**b**); Surface plot of electric field magnitude overlaid with electric field streamlines (*green traces*) originating in a 10 mm diameter sphere centered in E_{source}, 11 mm distant from the nanoESI spray tip (**c**). Potentials applied to electrodes are identical to those given in Fig. 3.5a, c

While it is only ions that produce the signals measured in MS and IMS, the presence of adventitious neutrals can produce undesirable effects in both instances. Neutral species place a larger load on the vacuum system (notably evaporating solvent droplets) and may undergo reactions with the ions of interest to produce unexpected species that complicate analysis [20]. Additionally, in the case of ion soft-landing, neutral impingement on the deposition surface negates the highly discriminatory nature of the ion selection prior to the surface collision.

In an attempt to address sensitivity and neutral transmission complications, a curved electrode system was constructed from a conductive polymer using a fused deposition modelling (FDM) 3D printer. The assembly is composed of a cylindrical source electrode region (E_{source}) with an inner diameter (ID) of 20 mm and a length of 30 mm, proceeded by 3 curved electrodes (E_n) with an ID of 15 mm and a swept angle of 45° around a 15 mm radius of curvature. All electrodes are separated by 3 mm with spacers printed in either acrylonitrile butadiene styrene (ABS) or polylactic acid (PLA). The design of this electrode assembly is such that ions produced via ESI within the source region are focused into a well-defined spot at the deposition surface. This is achieved through the application of appropriate potentials to separate electrode components. A direct line-of-sight from the ion source to the deposition surface is avoided by the curved design, as such, neutral solvent droplets are blocked from contaminating the deposition surface or the API of a mass spectrometer. The device is shown in Fig. 3.1 interfaced with the inlet of a mass spectrometer and is accompanied by a cutaway rendering which displays an overlay of simulated ion trajectories. The low-cost, wide availability, an ever-expanding selection of materials, and the rapid manner of production makes FDM the ideal manufacturing strategy by which parts such as these are produced. The entire assembly discussed in this chapter was constructed in under 3 h, including spacers and electrode components.

3.2.2 Simulations of Ion Motion

Simulations of ion trajectories within the device were performed with SIMION 8.0 (Scientific Instrument Services) and the included statistical diffusion simulation (SDS) algorithm [21]. At atmospheric pressure, it is not computationally efficient to utilize traditional hard-sphere collision models as the mean free path in air is $\sim$ 67 nm [22]. Instead, the SDS algorithm calculates ion motion based on ion mobility and a simulated diffusion in the form of "jumps" in a random direction at each time step, the magnitude of which is determined based on collision statistics [21]. A more detailed discussion of ion trajectory simulation at atmospheric pressure is given in Sect. 1.3. The workflow from design to simulation was inherently simplified through the use of the SL toolkit included with SIMION. Within the SL toolkit the user may import geometry in the form of stereolithography (.stl) files. The surface mesh defined by the .stl files is read by the SL tookit and used to generate potential array points. Through the use of a Runge Kutta iterative method, these points are used to solve for a scalable electric field, the basis of the simulation environment in SIMION. Because .stl is the native file format accepted by most software packages to prepare files for 3D printing, the same files may be used for both electrode production and trajectory simulation.

3.2.3 Imaging of Focused Ion Stream

The ability to generate, transmit, focus, and detect ions in air with the curved polymeric electrode system was demonstrated by spraying a mixture of tetraalkylammonium (TAA) bromide salts (10 μM in acetonitrile) from a nanoESI emitter into the source region (E_{source}) of the curved electrode. Images of ion intensity at the exit region of the curved electrode system were reconstructed from data obtained by scanning an IonCCD™ detector (OI Analytical, AL, USA) across the exit orifice of the final electrode. In brief, the IonCCD™ was mounted onto a computer controlled moving stage and the detector slit was scanned across the exit of the last electrode at a fixed rate of 0.1 mm/s with the detector integration time set to 100 ms. An illustration of this process is shown in Fig. 3.2.

Throughout this process a potential of 10 V was applied to the IonCCD™ housing. The application of this potential establishes a mild electric field in the space between the electrically floated detector array and the aluminum enclosure (0.711 mm). As a consequence ions are drawn to the detector surface which results in the observation of a more intense signal. A Matlab script was used to extract individual scans taken during the acquisition period and reconstruct these into 2D images of ion intensity on the basis of detector integration time and the moving stage velocity. These values were used to calculate position along the scan axis (Y(t)) for each detection cycle of the IonCCD™.

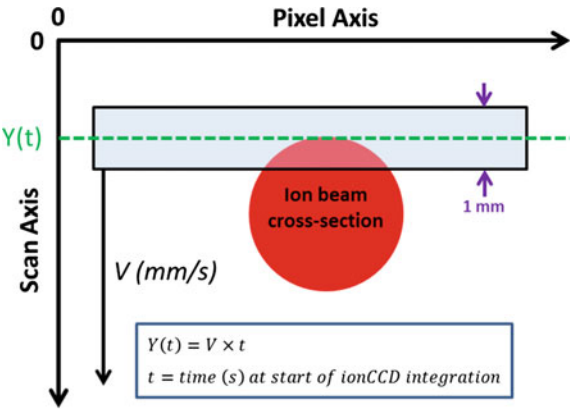

Fig. 3.2 Diagram illustrating how IonCCD™ data was captured and the data assembled into a 2D plot of ion intensity from individual integration time steps. The detector slit is indicated by the *blue* transparent box

3.2.4 Ion Transfer Efficiency

An experimental examination of ion transmission through the electrode system was performed by spraying a mixture of 10 μM tetrapropyl-, tetrabutyl-, tetrahexyl-, and tetradodecylammonium bromide in ACN through a pulled nanoESI emitter (5 μm tip) into the source region (E_{source}) of the device shown in Fig. 3.1b, c. A Keithley 6487 picoammeter was used to monitor the current impinging on an aluminum slide ($I_{surface}$), positioned 1 mm from the exit of E_3. The current measured at this surface was compared to the total spray current (I_{spray}). The magnitude of I_{spray} was determined by monitoring the voltage drop across a 4.7 MΩ resistor connected in series between the spray tip and high voltage source and calculating the current passing through the resistor from this value and the resistance, as determined by Ohm's Law. Unless otherwise noted, the spray tip was inserted 1 cm into E_{source} and potentials applied to each electrode were identical to those given in Fig. 3.5a-c.

3.2.5 Ion/Molecule Reactions

Ion/molecule reactions (IMR) have been shown to have great analytical utility, especially in the case of structural elucidation [23–25]. IMRs in the gas phase offer several benefits compared to their solution counterparts. Very little neutral reagent is required for an IMR and often the headspace vapor is sufficient to generate measurable product. Reaction rates and efficiencies are also inherently high for most IMRs, meaning that analytes in trace quantities will still form a detectable product [24]. This is especially true for IMRs performed at atmospheric pressure in IMS instruments, as the number of collisions per second is dramatically increased in comparison to the same reaction performed in an ion trap under vacuum [26]. However, the lack of straightforward identification of products in IMS generally requires the use of tandem IMS-MS instrumentation [26]. Often, significant

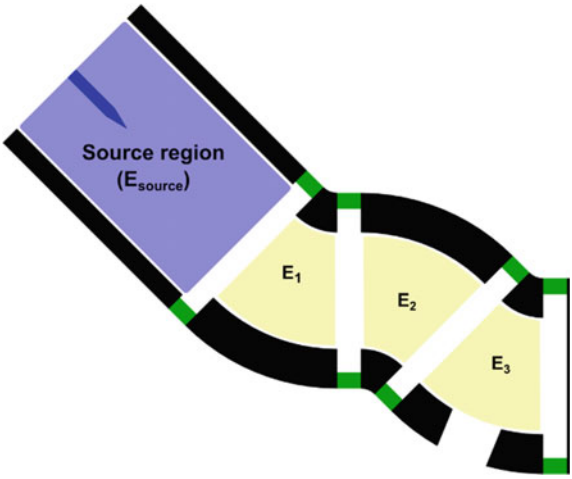

Fig. 3.3 Cutaway view of modified electrode system showing opening for neutral vapor introduction

modification to MS instruments must be made in order to perform ion/molecule reactions, which can be costly and time-consuming. The coupling of IMS to MS instruments suffers from similar drawbacks.

As a proof-of-concept demonstration of an ion-molecule reaction performed with the plastic electrode system in air. Protonated tert-butylamine and cyclohexylamine ions were generated by nanoESI from 10 ppm solutions in methanol. As these ions passed through the electrode system they were exposed to the vapor emanating from cotton swab saturated with a solution of 1000 µg/mL dimethyl methylphosphonate (DMMP) in the last region (E_3) of the electrode system shown in Fig. 3.3. In order to introduce DMMP vapor, the final electrode was replaced with an electrode having a hole through which the cotton swab could be inserted. A depiction of this is shown in Fig. 3.1a, however it should be noted that for IMR experiments the electrodes were arranged such that the final electrode (E_3) contained the hole and not E_2 as shown in Fig. 3.1a. Accurate positioning of the electrodes was performed by mounting the assembly to a 3 axis moving stage such that the exiting ions were sampled with the API of an LTQ linear ion trap (Thermo).

3.2.6 Separation of Ions in Air

The most common method of sorting ions in the gas-phase is on the basis of their mass-to-charge ratio (*m*/*z*) such as that performed in MS experiments. Alternatively, they may be separation based on an interaction with a background gas in the presence of well-defined electric fields as is done in IMS instruments. Separation based on *m*/*z* necessitates the use of a vacuum system, whereas a laminar flowing gas is used in the instance of an ion mobility separation performed at atmospheric pressure.

In an effort to demonstrate a simplified separation of ions in air without the use of a vacuum or a flowing gas, pulsed voltages were employed with the electrode system as a means to inject ions into the curved ion path and effect a separation of tetraalkylammonium (TAA) cations. Controlled injection of ions into the turning electrodes was accomplished by modifying the electrode system to include a region separated by two stainless steel woven wire meshes separated by 3 mm (ion injection region) as is shown in Fig. 3.4. A solution of 10 μM each of tetrapropyl-, tetrabutyl-, tetrahexyl-, and tetradodecylammonium bromide in ACN was sprayed with a nanoESI emitter into E_{source}. A floated high voltage pulse (2530 V high, 2480 V low) was applied to the mesh directly after the source region with the second mesh held flush to the opening of the first curved electrode to facilitate electrical contact with E_1. A pulse width of 50 ms with a repetition rate of 1 Hz was used for ion injection. Potentials applied to the nanoESI electrode, E_{source}, E_1, E_2, and E_3 were 4.50, 3.20, 2.50, 2.33, and 1.45 kV, respectively. Injected ion packets were sampled and analyzed by positioning the API of the MS to accept ions exiting E_3. The LTQ was operated with an injection time of 10 ms, giving an approximate repetition rate of 10 Hz.

A comparison of simulated ion separation under nearly identical conditions was also carried out. Because SIMION is ineffective at modeling ion behavior at ion sources, all ions were initiated within a uniform distribution between the mesh electrodes compromising the injection region. Initially the voltage on the mesh nearest the ion source was set to the high value used for injection (2530 V) for 50 ms, after this time it was lowered to match that used experimentally following an injection cycle (2480 V) for the remainder of the simulation. This approach does not accurately model the experimental ion distribution between the mesh electrodes during the injection, but is used for the purposes of simplification so that arrival times of ions at the detector (a mass spectrometer in this case) can be approximated to determine if simulation values are in rough agreement with experimental data.

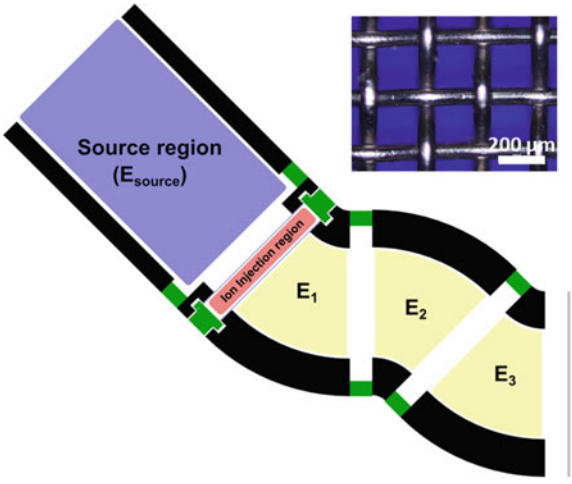

Fig. 3.4 Electrode system modified to allow time-resolved injection into the curved electrode region. An image of the mesh used is shown inset

3.3 Results and Discussion

3.3.1 Ambient Ion Focusing

When appropriate DC potentials are applied to the individual components of the electrode assembly, a strong focusing effect is observed. A similar effect has been previously observed in experiments in which a spray was generated within an ellipsoidal cavity held at kV potentials, positioned near a grounded surface [27]. The observation of this effect is due to the propensity of ions at atmospheric pressure to follow electric field streamlines when no external pneumatic forces are applied. This is illustrated through a comparison of predicted ion trajectories as shown in Fig. 3.1b and a plot of electric field streamlines originating in same region ions were initialized (Fig. 3.1c). As stated previously, the curvature of the ion path greatly reduces the probability of neutral transmission by avoiding line-of-sight from the sprayer to the detection/deposition surface. Such a geometry is difficult to machine by traditional subtractive manufacturing techniques, yet its production is trivial through additive manufacturing methods such as FDM.

A comparison of the experimentally measured ion intensity (reconstructed intensity plots) at the deposition surface and simulated ion distributions under identical conditions are shown in Fig. 3.5. The similarity between simulation results and experimental measurements show the predictive power of SIMION-SDS. The elongation seen in the reconstructed intensity plots as compared to the simulated 2D ion distribution at the electrode exit is likely a result of both the gap between aluminum housing and the detector surface as well as the width of the pixel array (1 mm). Specifically, elongation along the pixel axis may be the result of ion diffusion during transit of the 0.711 mm gap between the housing and detector surface. This is negated slightly by the application of a potential to the housing, but cannot be eliminated in entirety. Additionally, there are undoubtedly artifacts introduced by the width of the pixels (1 mm) which would contribute to the observed elongation along the scan axis in the reconstructed intensity map. As an example, with a scan rate of 0.1 mm/s and integration time of 100 ms, the detector moves approximately 0.1 mm during a detection cycle, which is only 10 % of the pixel width. Thus the intensity at each position along the scan axis includes the entirety of ions exiting the electrode ±500 μm from the assigned position, Y(t). Moreover, the true distribution of ions near the emitter tip is unknown and cannot be accurately modeled without complex treatment. In order to simplify the simulation ions were initiated with 3D Gaussian distribution (σ_{xyz} = 5 mm) in the source region and space-charge effects were not accounted for throughout ion transit. Gas velocity throughout the ion path was assumed to be static (no local gas flow). In spite of the simplified consideration of simulation conditions, ion intensities as simulated at the detection surface are in good agreement with experimental results, which highlights the utility of the SIMION-SDS algorithm in predicting the performance of the 3D printed polymeric electrodes.

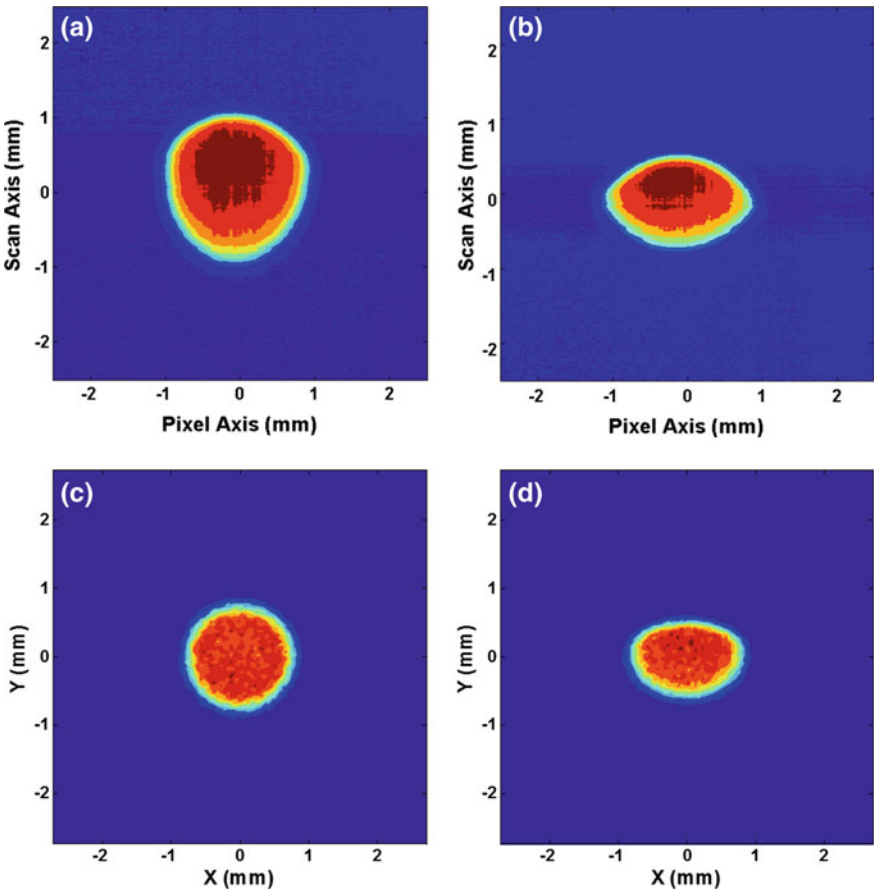

Fig. 3.5 Experimental (**a**–**b**) and simulated (**c**–**d**) tetraalkylammonium ion intensity at deposition surface for different electrode potentials. In (**a**) and (**c**) potentials on electrodes E_1, E_2, and E_3 were 2.90, 2.60, and 1.80 kV, respectively; In (**b**) and (**d**) potentials on electrodes E_1, E_2, and E_3 were 2.95, 2.12, and 1.77 kV, respectively. In each case E_{source} was set to 3.00 kV and spray potential was set at 4.65 kV

3.3.2 Ion Transfer Efficiency

The fraction of ions which traverse the entire device varies greatly, with a large dependence on the potentials applied to the electrodes in addition to the spray emitter. A summary of the results of transmission efficiency experiments is shown in Table 3.1.

Under most the most common operating conditions, such as those give in Fig. 3.5a, c, 1–10 % of the total spray current is transmitted to the detection surface. It is possible to increase transmission efficiency by iteratively tuning the potentials on each electrode as well as the spray tip. With the tip position maintained in the

Table 3.1 Efficiencies of ion transfer from spray tip to deposition surface under typical operating conditions. Potentials applied to E_{source}, E1, E2, and E3 are identical to Fig. 3.5a-c. Spray voltage is given as the difference of potential applied to the E_{source} and nanoESI spray tip

Spray voltage (kV)	I_{source} (nA)	$I_{surface}$ (nA)	Transmission efficiency (%)
0.750	3.52	0.28	7.8
1.00	19.65	0.50	2.5
1.25	37.99	0.67	1.8
1.50	56.56	0.75	1.3
1.65	67.70	0.87	1.3

same position as the data collected in Table 3.1 (inserted 1 cm into E_{source}) it was possible to transmit 11 % of an 11.10 nA current through the device. To achieve this, potentials of 3.89, 3.00, 2.64, 1.89, and 1.37 kV were applied to the spray tip, E_{source}, E_1, E_2, and E_3, respectively. While the ion distribution at the surface was not mapped under these conditions, simulations show a significant increase in spot size at the detection surface. By further adjustment of potentials and inserting the nanoESI emitter further into E_{source} (approximately 10 mm distant from the opening of E_1) a 55 % transmission of a 4.01 nA spray current was achieved. Potentials applied to the spray tip, E_{source}, E_1, E_2, and E_3 were 3.65, 2.50, 1.76, and 1.27 kV, respectively.

Simulations were used as the primary tool in determining where ion losses might occur within the devices. Under typical operating conditions as shown in Fig. 3.5a-c, a simulation was performed in which the ions were originated uniformly within a cylindrical volume extending from the tip of a nanoESI emitter (inserted 1 cm into E_{source} as is visible in Fig. 3.1c) to the exit of E_{source}. From this simulation an "acceptance volume" (defined as the volume within the source capable of transmitting ions to the deposition surface) was determined. The transmission efficiency was also calculated from the simulated trajectories of 4×10^4 ions (10^4 each of tetrapropyl-, tetrabutyl-, tetrahexyl-, and tetradodecylammonium cations) distributed uniformly within the cylindrical volume. The resulting acceptance volume is shown in Fig. 3.6a along with a plot of origin locations of all ions within acceptance volume in Fig. 3.6b. Electrode points and resulting deposition spot are shown as well.

From the calculated volumes of the ion origins and resulting acceptance volume a maximum transfer efficiency from ions originating only within E_{source} can be calculated as 40.5 %. This number assumes that ion generation occurs only within E_{source} which is not representative of the dynamic nature of spray ionization in which gas phase ions may be released from droplets projected beyond the confines of E_{source}. A qualitative examination of simulated ion trajectories suggests that the majority of losses occurs to the walls of E_{source} with minor losses to the walls of E_1. Ion losses within electrodes E_1–E_3 are assumed to be minimal and the transmission efficiency of more than 50 % achieved by positioning the spray tip within 10 mm of the entrance of E_1 supports this reasoning. It is expected that with further optimization of the size and shape of electrodes, transmission efficiency may be increased significantly.

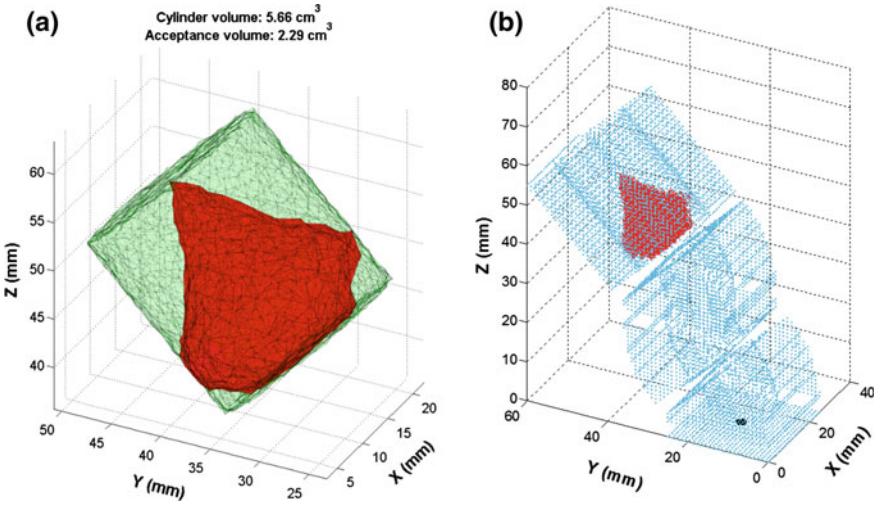

Fig. 3.6 Volume encompassing ion origin locations represented by *green mesh*, and acceptance volume represented by *red mesh* (**a**); 3D scatter plot showing origin location of ions within acceptance volume (*red points*), electrode points (*blue*), and resulting deposition spot (*black*) (**b**). Potentials applied to emitter and electrodes are identical to Fig. 3.5a-c

3.3.3 Ion/Molecule Reactions

When performing ion/molecule reactions within the final electrode the ion beam exiting the electrode structure was precisely aligned with the inlet of the MS. Once this alignment condition was established it was observed that the signal recorded by the mass spectrometer was largely independent of the position of the nanoESI spray tip within $E_{source.}$ This was realized by repositioning the spray tip with the 3 axis moving stage while recording MS spectra. Other than cases in which the spray tip was removed from E_{source} or moved to within 1–2 mm of the electrode walls, MS spectra and intensities remained unchanged. This effect has potential utility in decoupling spray position from recorded intensities to improve reproducibility when changing spray tips.

Mass spectra of the ion/molecule reactions between protonated cyclohexylamine and tert-butylamine ions with DMMP vapor as sampled from the final region of the polymeric electrode assembly are shown in Fig. 3.7. Similar IMRs using analogs of DMMP have previously been demonstrated for the identification of amino functionalities in a Fourier transform ion cyclotron resonance (FT-ICR) mass spectrometer [28]. These reactions highlight the potential usefulness of ion manipulation outside the mass spectrometer in exploring ion/molecule reactions for functional group identification. The ability to perform and interrogate these reactions outside the MS may allow for a condition in which an ion separation is performed at atmospheric pressure after a reaction has taken place to identify the presence of a target compound in the analyte mixture.

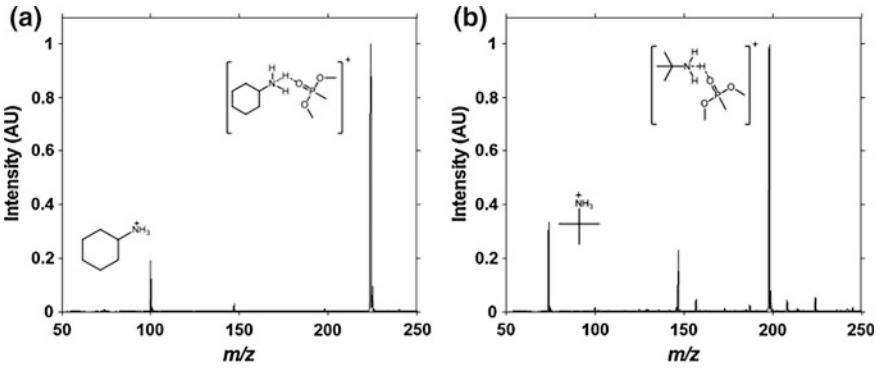

Fig. 3.7 Mass spectra showing reaction of protonated cyclohexylamine with DMMP vapor (**a**) and tert-butylamine with DMMP vapor (**b**)

3.3.4 Separation of Ions in Air

The time-resolved separation of TAA cations was demonstrated in the manner outlined in Sect. 3.2.6. The results of these scans are shown in Fig. 3.8a. Because ion injection into the trap of the MS was not synchronized with injection into the curved electrode system, the comparison between detection times on the LTQ mass spectrometer to simulation results is only a qualitative measure of the observed separation effect on the same time scale as that observed experimentally. Simulation results shown in Fig. 3.8b suggest that a time resolved separation of *m*/*z* 691 and *m*/*z* 354 from the lower mass TAA cations should be evident in the mass spectra. The observed results show that this is indeed the case, confirming simulation results.

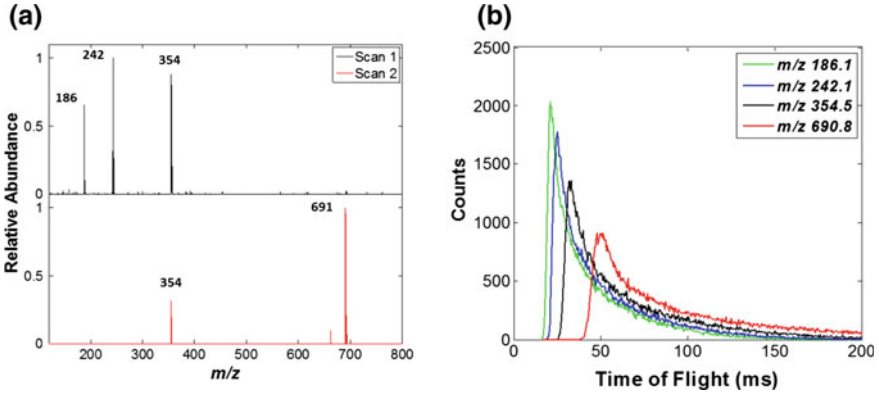

Fig. 3.8 Spectra of tetraalkylammonium cations from consecutive MS scans (**a**); Simulated time of flight distribution for tetraalkylammonium cation mixture transmitted through printed electrode assembly (**b**)

This proof-of-concept demonstration shows the ability to separate gas-phase ions in air and is meant to highlight a potential use of the 3D printed electrodes as a better resolved separation is surely possible through optimization of applied potentials, ion injection parameters, and electrode geometries.

3.4 Conclusions

Through the use of commonly available, and inexpensive additive manufacturing methods, a system of small plastic electrodes was developed with unique applications in fields relating to mass spectrometry and ion mobility. In particular, the ability of such a system to focus, transport, and even separate ions using only the electric fields was shown. Additionally, the apparatus was used as a reaction vessel to perform ion-molecule reactions, which were subsequently analyzed by a mass spectrometer. The only forces acting on the ions are their initial energies associated with sprayed droplets—which are not pneumatically assisted—and the forces due to the static electric fields. It is also noted that the degree of solvation of the ions (if any) remains unknown. The modest separation of ions demonstrated in the simple, low-cost system suggests that through optimization, a device may be constructed in which ions may be purified through soft-landing or directly analyzed, all without the constraints of a vacuum system or well defined gas flow. Moreover, the detection and two dimensional profiling of the ion beam under ambient conditions, combined with the low cost of electrode production, may pave the way for distinct surface patterning with unorthodox electrode geometries.

References

1. R.G. Cooks, A.K. Jarmusch, M. Wleklinski, Int. J. Mass Spectrom. **377**, 709–718 (2014)
2. S.J.E.-J. Kojo, *High-Throughput Analysis in the Pharmaceutical Industry*, Editon edn. (CRC Press, Boca Raton, 2008), pp. 377–391
3. R. Aebersold, M. Mann, Nature **422**, 198–207 (2003)
4. W.E. Parkins, Phys. Today **58**, 45–51 (2005)
5. G.E. Johnson, Q. Hu, J. Laskin, Ann. Rev. Anal. Chem. **4**, 83–104 (2011)
6. M.E. Monge, G.A. Harris, P. Dwivedi, F.M. Fernández, Chem. Rev. **113**, 2269–2308 (2013)
7. Z. Ouyang, R.G. Cooks, Ann. Rev. Anal. Chem. **2**, 187–214 (2009)
8. F. Lanucara, S.W. Holman, C.J. Gray, C.E. Eyers, Nat. Chem. **6**, 281–294 (2014)
9. G.A. Eiceman, Z. Karpas, H.H. Hill, *Ion Mobility Spectrometry*, 3rd edn. (Taylor and Francis, Hoboken, 2013)
10. J. Orloff, *Handbook of Charge Particle Optics*, 2nd edn. (Taylor and Francis, Hoboken, 2008)
11. M. Reiser, *Theory and Design of Charged Particle Beams*, 2nd edn. (Wiley-VHC, Weinheim, 2008)
12. A. Badu-Tawiah, D. Campbell, R.G. Cooks, J. Am. Soc. Mass Spectrom. **23**, 1077–1084 (2012)
13. A. Badu-Tawiah, J. Cyriac, R.G. Cooks, J. Am. Soc. Mass Spectrom. **23**, 842–849 (2012)
14. A. Li, Q. Luo, S.-J. Park, R.G. Cooks, Angew. Chem. Int. Ed. **53**, 3147–3150 (2014)

15. H. Chen, L.S. Eberlin, R.G. Cooks, J. Am. Chem. Soc. **129**, 5880–5886 (2007)
16. J.B. Fenn, M. Mann, C.K. Meng, S.F. Wong, C.M. Whitehouse, Mass Spectrom. Rev. **9**, 37–70 (1990)
17. N.B. Cech, C.G. Enke, Mass Spectrom. Rev. **20**, 362–387 (2001)
18. J. Cyriac, T. Pradeep, H. Kang, R. Souda, R.G. Cooks, Chem. Rev. **112**, 5356–5411 (2012)
19. O. Hadjar, P. Wang, J.H. Futrell, Y. Dessiaterik, Z. Zhu, J.P. Cowin, M.J. Iedema, J. Laskin, Anal. Chem. **79**, 6566–6574 (2007)
20. B.C. Owen, T.M. Jarrell, J.C. Schwartz, R. Oglesbee, M. Carlsen, E.F. Archibold, H.I. Kenttämaa, Anal. Chem. **85**, 11284–11290 (2013)
21. A.D. Appelhans, D.A. Dahl, Int. J. Mass Spectrom. **244**, 1–14 (2005)
22. S.G. Jennings, J. Aerosol Sci. **19**, 159–166 (1988)
23. S. Osburn, V. Ryzhov, Anal. Chem. **85**, 769–778 (2012)
24. J.S. Brodbelt, Mass Spectrom. Rev. **16**, 91–110 (1997)
25. M.N. Eberlin, Mass Spectrom. Rev. **16**, 113–144 (1997)
26. A.E. Gary, A.S. John, *Practical Aspects of Trapped Ion Mass Spectrometry*, vol. V, Editon edn. (CRC Press, Boca Raton, 2009), pp. 387–415
27. Z. Baird, W.-P. Peng, R.G. Cooks, Int. J. Mass Spectrom. **330–332**, 277–284 (2012)
28. M. Fu, R.J. Eismin, P. Duan, S. Li, H.I. Kenttämaa, Int. J. Mass Spectrom. **282**, 77–84 (2009)

Chapter 4
3D Printed Annular Focusing Ambient Ion Mobility Spectrometer

4.1 Introduction

From its beginnings as "Plasma Chromatography™" for the analysis of trace organic molecules [1–4], to applications in security for the detection of explosives [5–7] and chemical warfare agents [8–10], and more recent applications in structural analysis of biomolecules [11–14], ion mobility spectrometry (IMS) has been demonstrated as a powerful analytical tool. The utility of IMS lies largely in its ability to distinguish structural and conformational differences between ion populations and the rapid manner in which ions may be separated from complex mixtures [15]. This utility is further enhanced through the coupling of IMS with MS, for enriched information output [16, 17]. One particular advantage of IMS is the wide range of pressure regimes under which it may be operated, ranging from <1 Torr to atmospheric pressure conditions [18].

There are several different embodiments of IMS, each of which separates gas-phase ions based on their electrophoretic mobility through a drift gas [19]. High-field asymmetric ion mobility spectrometry (FAIMS) [10, 20] and differential mobility analysis (DMA) [21, 22] are two techniques normally performed under atmospheric pressure that provide a continuously filtered stream of mobility-selected ions. In both FAIMS and DMA ions are carried by a laminar flow of drift gas between parallel plate electrodes, often constructed as a set of coaxial cylinders [23, 24]. The distinction between FAIMS and DMA lies in the electric field applied to the electrodes. Additionally, the separation between electrode plates is typically no larger than 2 mm in FAIMS instruments, whereas typical separation between plates within DMA instruments is much larger.

Separation in FAIMS is achieved by applying an asymmetric waveform (peak voltages over a single period must be opposite, but unequal in magnitude), to one electrode while a compensation voltage (CV) is applied to the opposite electrode [20]. The asymmetry of the waveform must be such that the high field portion is significantly greater than the low field and an integration of the waveform over one

Z. Baird, *Manipulation and Characterization of Electrosprayed Ions Under Ambient Conditions*, Springer Theses, DOI 10.1007/978-3-319-49869-0_4

period is equal to zero [25]. As ions are carried by the drift gas through the analysis region, they are separated based on differences in mobility under high- and low-field conditions. Through selection of an appropriate CV, a particular ion will achieve a balanced condition and exhibit a stable trajectory through the entirety of the device and will be detected.

DMA employs a similar configuration of parallel plate electrodes, but rather than a waveform, a DC voltage is applied to one electrode while the other is grounded. Ions are introduced into the analyzer region through a narrow opening in the grounded outer plate and are carried by a laminar flow of gas, between the parallel electrodes [26]. Throughout this transit ions migrate toward the inner electrode at different velocities, depending on the mobility of the ion in the carrier gas and the voltage applied to the electrode. Ions are sampled downstream of the gas flow through a slit (detector region) in the inner electrode. Only ions with a particular velocity will be sampled through this slit, their identities dependent on gas velocity and electric field strength as ions are effectively separated spatially within the DMA [24]. Because of this, the linear distance between the ion introduction region and the detector region is of critical importance in determining the collisional cross-section of a sampled ion, a property directly related to the ion's size and conformation. Spectra are collected by scanning the applied potential on the central electrode.

Unlike DMA and FAIMS, drift tube ion mobility spectrometry (DT-IMS) separates a packet of ions temporally as they traverse a drift region [18]. The drift region is normally composed of a series of axially aligned, open-ring electrodes, to which a DC potential gradient is applied, thus creating a near-uniform electric field extending along the length of the drift tube. Drift tubes have also been constructed using monolithic resistive glass cylinders [27], rather than stacked rings. Upon injection into the drift region, ions are propelled along the length of the drift tube by the electric field. Ions traverse the length of the drift tube at different velocities, determined by their mobility in the drift gas [28], and are detected in a time resolved fashion, to construct an ion mobility spectrum.

More recently, travelling wave ion mobility spectrometry (TW-IMS) [29] which uses a stacked ring configuration similar to DT-IMS, has seen widespread adoption. In TW-IMS, a confining RF voltage is applied 180° out of phase to adjacent electrodes onto which voltage pulses are superimposed in a step-wise serial manner to generate potential "waves", thus propelling ions along the drift tube where they are separated temporally [30]. Unlike other IMS approaches mentioned, TW-IMS is restricted to operation at pressures around 0.1–3 Torr [29, 31]. TW-IMS allows for high duty cycles and relative ease in coupling with MS instruments [29], but is electronically complex compared to DT-IMS.

As previously stated, one of the main advantages of IMS techniques is the ability to relate IMS spectra to conformation and size of ions. In the case of FAIMS, this relation is only known empirically due to the complex behavior of ions in a rapidly changing electric field. On the other hand, DMA is routinely used to size aerosol particles as the separation parameters can be directly correlated to size so long as the gas flow is well controlled and the electric field is well-defined [32]; however,

due to Brownian motion, resolution is relatively poor for ions smaller than ~10 nm, even in specially designed analyzers [24].

Collisional cross section (CCS) measurements, a property directly correlated to an ion's size and conformation, are often performed by DT-IMS as the velocity of an ion in a uniform electric field in the presence of a drift gas is well established [28, 33]. TW-IMS instruments may also be used to measure CCS, however the relationship of ion velocity to CCS is not as straightforward as in DT-IMS. Because of this, CCS standards of known mobility must be used to calibrate CCS measurement by TW-IMS instruments [34, 35].

The simplicity of DT-IMS instrumentation, combined with its wide operational pressure regime make it a good candidate in the analysis of size and conformation at a number of different conditions. In light of this, an effort was undertaken to construct a 3D printable, plastic DT-IMS for operation at ambient conditions that was easily interfaced with nanoESI. The drift tube employs a novel electrode geometry which serves to focus nanoelectrosprayed ions into an annulus, while simultaneously blocking the transmission of neutral droplets, without the use of supplementary gas flow or heating. SIMION-SDS simulations were used to explore electrode geometries and the results compared with experimental data. This approach is demonstrated as a viable rapid, low-cost alternative to traditional manufacture of IMS drift cells.

4.2 Experimental

4.2.1 Ion Trajectory Simulations

SIMION-SDS simulations were used as the primary tool for exploring different electrode configurations and dimensions. For a detailed discussion of the SDS algorithm within the SIMION environment, see Sect. 1.3. Electrode geometries were constructed in the script-based geometry (.GEM) file format such that the density of the potential array points and electrode dimensions could be varied parametrically. Through the use of the GEM format it was possible to simplify the simulation environment to be cylindrically symmetric, thus solutions to the electric fields and resulting trajectory simulations were reduced in computational complexity. Simplification of the electrode geometry in such a manner does not allow for perfect representation of the true experimental setup, but serves to explore the feasibility of different electrode dimensions.

Unless otherwise stated, simulations used a potential array grid unit (GU) density of 0.04 mm/GU and a trajectory quality setting of zero. This means that time steps within the simulation are fixed such that integration steps occur over the distance of one GU. All simulations were performed neglecting the effects of space-charge. The reduced mobilities (K_0) and masses of, tetrabutyl-, tetrahexyl-, tetraoctyl-, and tetradodecylammonium cations were specified within the simulation

environment and the effective diameter of each was estimated from this data by the SDS algorithm. Each simulation was performed at atmospheric pressure (760 Torr) in air at 25 °C with no bulk gas flow.

4.2.2 *Device Design and Construction*

4.2.2.1 Description of Device

A cross-section of the full 3D printed IMS device is shown Fig. 4.1. In brief, the device consists of 3 regions: the source region (section (a), highlighted in orange), the ion injection region (section (b), highlighted in blue), and the drift region (section (c), highlighted in green). The source region consists of an 3D printed open outer cylinder with an inner diameter of 30 mm and a neutral blocking disk with an outer diameter of 15 mm and a thickness of 1.6 mm. Like the drift rings discussed in the following paragraph, this central disc is connected to the outer walls of the cylinder by 3 filaments, each 0.7 mm wide. A nanoESI tip is placed within the open end of the source region and for most experiments was located 5–15 mm distant from the neutral blocking disk.

The injection region is composed of a ring electrode and a stainless steel mesh held in contact with a ring electrode identical to the drift rings and is separated from

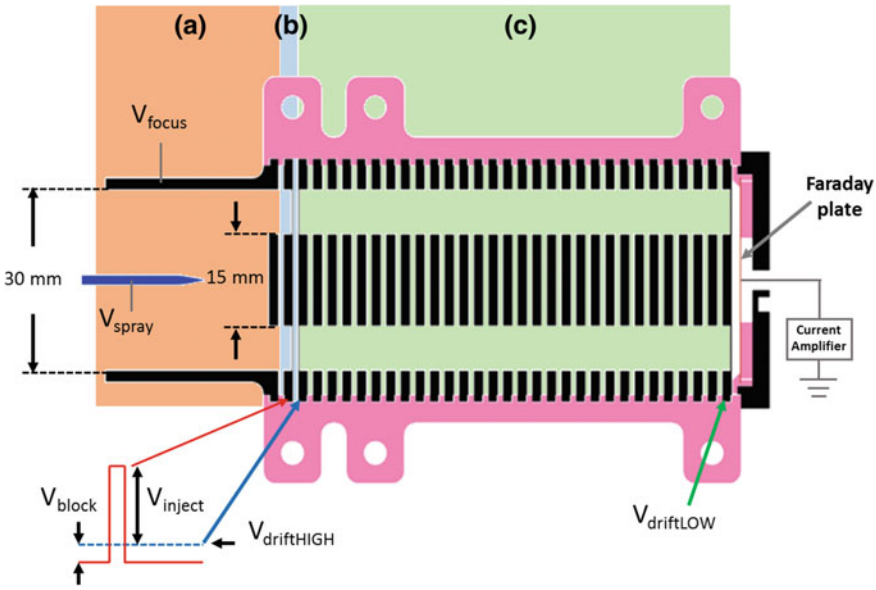

Fig. 4.1 Cross-section view of 3D printed IMS showing the source regions (**a**), injection region (**b**), and drift region (**c**). The injection waveform is shown in the *bottom-left* of the figure

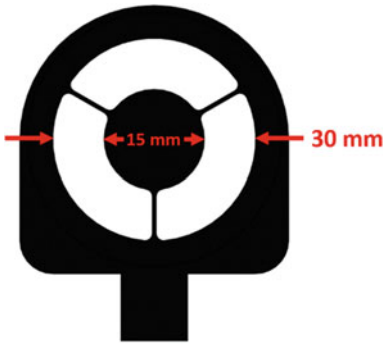

Fig. 4.2 Top-down view of drift ring electrode design

the first electrode of the drift region by a 0.96 mm thick PLA spacer ring. A top-down view which highlights the design features of the drift ring electrodes is shown in Fig. 4.2.

The drift region consists of a series of 30 identical open rings with an inner diameter of 30 mm for a total drift length of 75.84 mm. Each drift ring has a central coaxial disc with an outer diameter of 15 mm. The central discs are connected to the outer rings by 3 filaments 0.7 mm wide. A stainless steel mesh is held flush with the opening of each end of the drift region. These meshes serve to limit electric field perturbations from the injection waveform and to shield the detector from image current arising due to approaching ion packets. A Faraday plate detector consisting of a copper disc was placed 1.6 mm distant from the final mesh.

All stainless steel meshes, including that used in the injection region, were purchased as sheets from E-Fab (Santa Clara, CA, USA). Each mesh is 80 μm thick and contains 500 μm wide hexagonal openings with 76 μm webbing (69% open). The meshes were cut by hand to appropriate shapes using a normal pair of scissors.

Drift rings, stainless steel meshes, and the source electrode are all held in a 3D printed housing made of polylactide (PLA). The design of the housing is such that electrodes are held at defined spacing (0.96 mm) for an electrode pitch of 2.56 mm. The incorporation of spacers in the structure of the housing simplifies the construction of the device and reduces multiplicative errors from individual spacer height variations. The Faraday plate detector is separated from the terminal mesh of the drift region by a PLA spacer and is held in place by a screw-on conductive plastic piece. This piece is grounded to electrically shield the Faraday plate.

The rounded-rectangular portion of the electrode (see Fig. 4.2) is designed to slide into slots within the housing for a secure fit. The rectangular extension seen in the lower portion of the figure extends through the housing and has a small cylindrical opening, into which header pins are inserted for electrical connections to different components of the IMS. An image of a single ring electrode inserted into one side of the PLA/PHA housing is shown in the right image of Fig. 4.3.

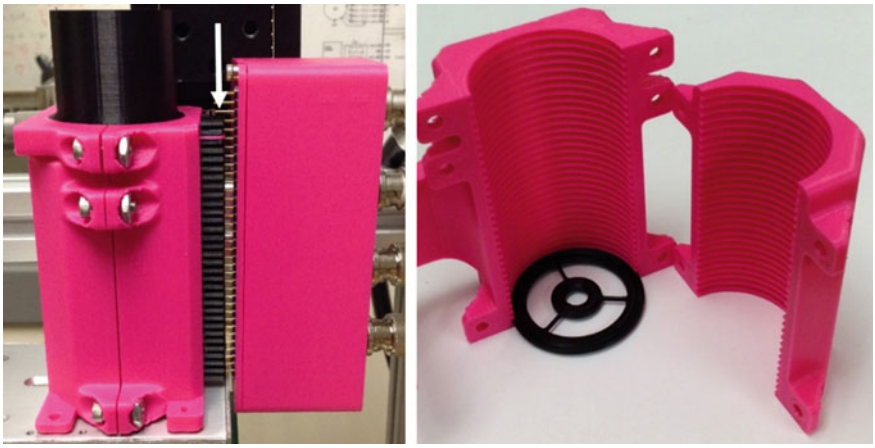

Fig. 4.3 IMS assembly with electrical connections to electrodes through header insertion (*left*) and electrode housing showing integrated spacers and method of electrode insertion (*right*). Electrical connections made with header are indicated by the *white arrow*

4.2.2.2 3D Printed Components

All electrodes (other than the stainless steel meshes) and housing components were first modeled in Autodesk Inventor, exported in .stl format and 3D printed by fused deposition modeling (FDM). See Sect. 1.4 for details of the FDM process. Electrodes were printed in a polyethylene terephthalate glycol copolymer (PETG) sold under the name 3DXNano ESD PETG (3DXTech, MI, USA). The filament contains a dispersion of multi-walled carbon nanotubes (MWCNTs) which serve to provide a slight conductivity to the PETG. According to the manufacturer, surface conductivity of the final 3D printed components generally falls in the range of 10^7–10^9 Ω/square. This range of conductivity is normally associated with materials made for applications in which electrostatic discharging (ESD) is a necessity. Electrodes were printed on a modified Makerfarm Prusa i3v (Makerfarm, UT, USA). The modifications were made to improve print quality and to permit direct-drive extrusion with an E3D v5 all-metal hot end (E3D, Oxfordshire, UK). For the manufacture of electrodes, the hot end was fit with a 0.25 mm brass nozzle. All non-conductive components were printed in a polylactide/polyhydroxyalkanoate (PLA/PHA) blend (Colorfabb, Venlo, Netherlands) on the same Makerfarm Prusa i3v. All housing and non-conductive components were printed using a 0.4 mm nozzle.

G-code was generated from .stl files in Slic3r version 1.2.9. General slicer settings for conductive PETG components were: 0.16 mm layer heights, 3 perimeters loops, 20% hexagonal infill, 250 °C extrusion temperature, and 80 °C

bed temperature. All parts printed in PLA/PHA were printed at 0.2 mm layer height, 3 perimeters, 25% rectilinear infill, 195 °C extrusion temperature, and 70 °C bed temperature. Both materials were printed onto a glass bed coated with a layer of polyimide tape that was wiped clean with acetone to remove oils and any other contaminants.

4.2.2.3 Electronics

Electrical contact to individual electrodes is accomplished by inserting the pins of a 0.100 inch (2.56 mm) pitch header into holes in the tabs extending through the housing. A picture of this connection is shown in the left image of Fig. 4.3. The potential on the source electrode (E_{source}) is controlled by a Spellman SL10 high voltage power supply (Spellman High Voltage, NY, USA).

Ion injection into the drift region is facilitated by the application of a floated high voltage pulse to the injection mesh/electrode. The high and low levels of the pulse are controlled by a homebuilt high voltage power supply, connected to a GHTS 60 A push-pull switching unit (Behlke, MA, USA). Timing of the injection pulses was controlled by a DG535 digital delay/pulse generator (Stanford Research Systems, Inc., CA, USA). The voltage gradient within the drift region of the IMS is supplied by connecting electrodes to different probe points along a resistor chain constructed from 1.0 MΩ precision resistors (TE Connectivity, PA, USA). The voltage at each end along the resistor chain ($V_{driftHIGH}$ and $V_{driftLOW}$ in Fig. 4.1) is controlled by a homebuilt high voltage power supply. The resistor chain and high voltage lines are housed in a 3D printed PLA/PHA housing with MHV connections for input voltages. The entire drift tube assembly, with associated electronics is shown in the left image of Fig. 4.3.

The Faraday plate at the terminus of the drift region is connected to a Keithley 428 current amplifier (Keithley Instruments, OH, USA) and the inverting output is recorded on Tektronix TDS 2024C 4-channel oscilloscope (Tektronix, OR, USA). Signal acquisition on the oscilloscope is triggered on the injection pulse.

4.2.2.4 Operational Parameters of 3D Printed IMS

Control of the IMS makes use of 5 different voltage inputs and timed square wave pulses for ion injection. In each experiment performed with the 3D printed IMS, potentials applied to the emitter (V_{spray}), focusing electrode (V_{focus}), first drift ring ($V_{driftHIGH}$), and final drift ring ($V_{driftLOW}$) were 4500, 2500, 2000, and 300 V, respectively. During ion injection pulses the voltage on the injection electrode was either 50 or 100 V, relative to $V_{driftHIGH}$. At all other times the voltage of this electrode was −25 V, relative to $V_{driftHigh}$ (V_{block}). For all experiments, ions were gated into the drift tube at a repetition rate of 10 Hz.

4.2.3 Ion Deposition Image Collection

An IonCCD™ detector (OI Analytical, AL, USA) was used to examine the profiles of ion intensity on a deposition surface. In these cases, the IonCCD™ was mounted onto an automated XY moving stage (Dover Motion, MA, USA). The stage was then scanned at a fixed rate across the ion stream as it exited the electrodes. The intensities from IonCCD™ line scans were then reconstructed into two dimensional images of the ion plume at the deposition surface using a custom Matlab script. The script considers both the timestamps from the individual detection periods and the velocity of the moving stage when reconstructing an image. This process is illustrated in Fig. 3.2.

For experiments discussed in this chapter, the integration time of the IonCCD™ was set to 100 ms and the detector was scanned across the ion plume at a rate of 0.5 mm/s. Examination of the annular focusing effects within the source region uses neat acetonitrile (ACN) as the spray solution. In other cases, a 10 μM equimolar mixture of, tetrabutyl- (TBAB), tetrahexyl- (THAB), tetraoctyl- (TOAB), and tetradodecylammonium bromide (TDDAB) in ACN was used as the spray solution. For IMS separation, an 2 mM equimolar mixture of TBAB, THAB, TOAB, and TDDAB in ACN was used as the spray solvent.

4.2.4 Ion Transmission Efficiency

An evaluation of the efficiency of ion transfer from the nanoESI spray tip to the deposition surface is performed in a manner similar to that discussed in Sect. 3.2.4. Briefly, a 4.7 MΩ resistor is placed in series with the nanoESI spray tip and the voltage drop across this resistor is used to calculate the total spray current using Ohm's Law. This is compared to readings taken simultaneously at the deposition surface with a Keithley 6487 picoammeter (Keithley Instruments, OH, USA).

4.3 Results and Discussion

4.3.1 Annular Ion Focusing

The exploration in the use of concentric cylindrical electrodes is the result of experimental observations made during experiments with the ellipsoidal electrode design discussed in Chap. 2 [36]. By placing a series of open cylindrical electrodes inside the elliptical assembly and appropriately adjusting the potentials applied to each component, a condition was established in which an electrosprayed dye was deposited in an annulus with very narrow line-width. Traditional machining of such a device is a fairly complex and costly endeavor, as such, experimental tests of this

effect were not performed for some time. With the addition of a 3D printer to the laboratory and the development of methods for constructing suitable ion lenses through FDM methods [37], the exploration of this annular focusing effect through experiment became a trivial manner.

Initial explorations of electrode configurations were explored with SIMION-SDS simulations to gain a better understanding of the geometries necessary to generate the annular focusing effect. The electrode configurations considered for testing were limited to those that would be most accurately produced by FDM manufacturing methods. Despite the many advantages of additive manufacturing techniques such as FDM, there are limitations that must be considered. Because FDM relies on the sequential deposition of layered materials, there must be a surface on which to extrude subsequent layers. As such, overhanging structures must either be minimized in the design, or a support material printed underneath that is later removed (a strategy which introduces extra dimensional errors). In light of this, only electrode designs that could be manufactured without support material were tested in simulations before device manufacture.

The final electrode design consists of an outer cylinder with a coaxial disc placed flush with the exit plane of the cylinder. Ultimately, this was used as the source region of the IMS and its dimensions are detailed in Fig. 4.1. Simulations of the annular focusing effect were performed in which a potential of 1.5 kV was applied to the outer cylinder and central disc, and ions deposition location was monitored on a grounded, flat electrode located 1.6 mm distant from the opening plane of the focusing electrode. The resultant simulated ion trajectories and final deposition locations of protonated ACN ions that were originated from different points within the focusing electrode are shown in Fig. 4.4.

From the simulations shown in Fig. 4.4 it is evident that the points of origin have an impact on the focal distribution of the ion cloud within the apparatus. This is not problematic in the current embodiment of the system as ions are not generated within the entire volume of the electrode. Instead, ions originate from the tip of the nanoESI emitter, which is placed at a desired location within the cylindrical lens. This setup does not produce a true point-source for the generation of ions due to the initial expansion of the ESI plume and subsequent ionization events from progeny droplets; however, ion origins are still confined to a limited volume within the electrode. An important result of these simulations is the apparent ability to focus ions into an annulus with a line width of approximately 200 μm, even in the case when ions are originated across the entire 15 mm radius of the cylindrical electrode, ~1 cm distant from the central disc. Additionally, ions originating near the center of the electrode, 1 mm from this disc, are also drawn into this annulus rather than colliding with electrode. These points are of important note when considering the placement of a nanoESI emitter within the apparatus for the generation of ions.

These focal effects were experimentally verified by electrospraying ACN from a nanoESI emitter placed within a 3D printed electrode as previously described. Maps of ion intensity at the exit plane of the electrode were reconstructed from IonCCD™ scans as described in Sect. 4.2.3. A range of potentials were applied to the focusing apparatus and the spray emitter to determine the effects of each on the final focus

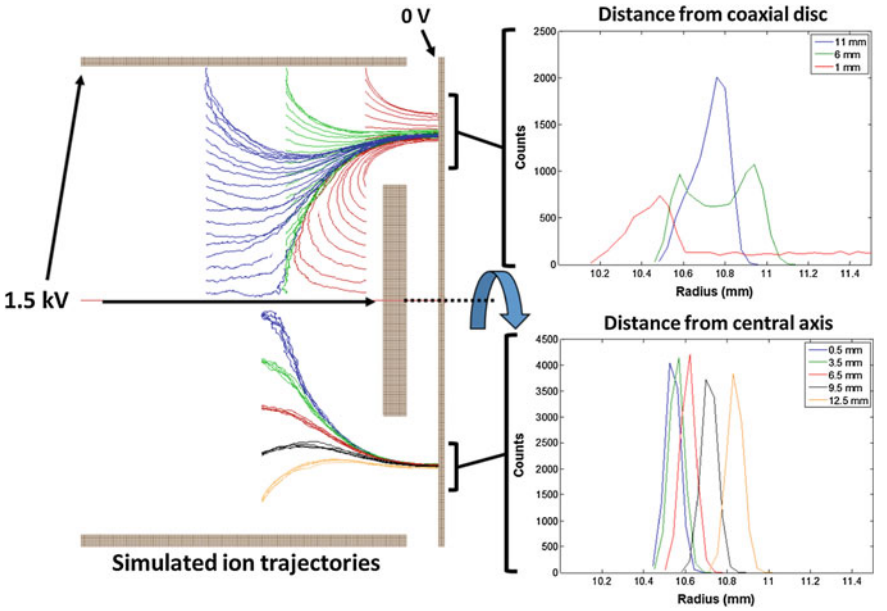

Fig. 4.4 Trajectories of protonated ACN ions from different origins (*left*) and radial deposition profiles from different ion origin locations (*right*). The *dashed line* denotes the axis of cylindrical symmetry within the simulation environment

and intensity of the ions exiting the focusing electrode. During these experiments the tip of the nanoESI emitter was placed coaxially within the outer cylindrical electrode and the tip was held 10 mm distant from the central disc. This placement was chosen based on the previously discussed simulation results. An illustration of the setup is shown inset of Fig. 4.5b. For imaging experiments, the silver disc (inset Fig. 4.5b) is replaced with an IonCCD™ detector mounted on a computer-controlled moving platform. It is important to note the presence of the 0.7 mm wide filaments connecting the central disc to the outer cylinder. These are necessary for manufacture of the electrodes and to assure uniform potential application to each component (the outer cylinder and coaxial disc). Simulations did not take these into account as the model was simplified to maintain axial symmetry.

In order to better characterize the annular focus, the reconstructed 2D images of ion intensity were subject to additional processing. Briefly, the intensity maps were converted to grayscale images and a threshold was applied at 40% of the maximum image intensity. A scatter plot was generated with each point corresponding to the location of a pixel whose value was above the 40% threshold and the data was then fit to a circle using a Landau-Smith algorithm [38]. The circular fit was then used to center all data from the original reconstructed image and intensities were normalized by subtracting the minimum intensity from each pixel within the original data. A representative centered and normalized image is shown in Fig. 4.5b. A table of position data was then constructed such that the intensity value in each pixel was

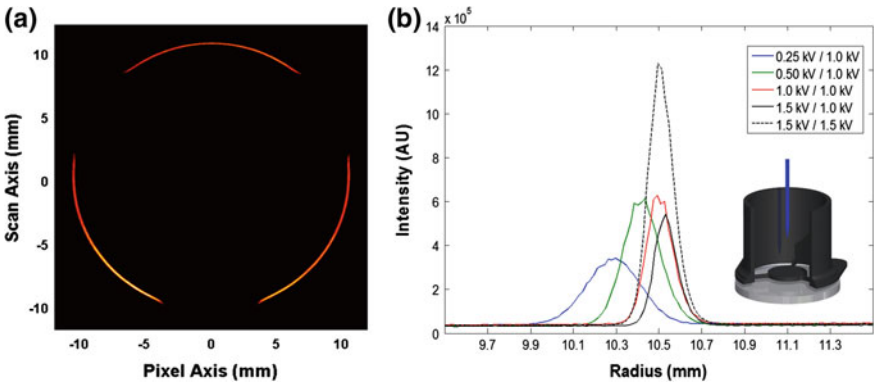

Fig. 4.5 Ion intensity map of annularly focused ions following image centering and normalization for an emitter potential of 3.0 kV and focusing potential of 1.5 kV (**a**), radial distribution of focused ions under different emitter and focusing voltages (**b**). Potentials applied to nanoESI emitter and focusing electrode are denoted in the legend of (**b**). Values are given as spray/focusing potential, where spray potential is relative to focusing potential (i.e. in the case of 0.25 kV/1.0, 1.25 kV was applied to emitter and 1.0 kV was applied to focusing electrode). In each case ions were generated by nanoESI of ACN solution

taken as the number of individual points at the corresponding location within the centered image. This table of position information was then transformed to polar coordinates and a histogram of radial deposition locations was constructed for each data set. The radial distribution of ions under different spray and focusing potentials is shown in Fig. 4.5a.

These results clearly illustrate the annular focusing, predicted by simulations. Through a comparison of the simulation results of ion origins, shown in the lower right portion of Fig. 4.4, it is expected that ions are indeed originating entirely from the central portion of the electrode and expansion of the ion plume is not deleterious to ion focusing. A contributing factor may be the initial dispersion of the ion plume into an annulus, thus spreading the generated charge over a larger volume, limiting the effects of space charge.

4.3.2 Annularly Focused Ion Mobility Spectrometer

The ability to focus electrosprayed ions into an annulus at atmospheric pressure, opens up the opportunity for a unique design of ion mobility drift tube which uses the same configuration of inner and outer electrodes throughout the drift region. One such advantage of this design is the ability to first focus ions into a region of uniform electric field (a necessity for optimal IMS separations) before injection into the drift cell, thus limiting the peak broadening associated with edge-effects in traditional drift tube design [27, 39]. Furthermore, the low cost associated with

FDM manufacture of the device components and wide availability of materials have the potential to expand the use of IMS instrumentation of this nature to laboratories otherwise unable to utilize such characterization methods. With these advantages in mind, the design detailed in Sect. 4.2.2 was constructed and the performance tested.

In general, ion separation within a DT-IMS involves 4 steps: (1) the production of gas-phase ions in the source region, (2) an injection of an ion packet into the drift region, (3) separation of the ions by a uniform electric field as they traverse a drift tube, and (4) the detection of separated ion packets. For these experiments, nanoESI was chosen as the means to generate ions as it is easily coupled with the annular focusing electrode and the annular focusing effect was well characterized. Injection of ion packets into the drift region was accomplished by applying a high voltage pulse to the injection mesh as illustrated in the lower left portion of Fig. 4.1. Upon passing the mesh at the entrance to the drift tube (see Fig. 4.1), ion packets are propelled along the drift tube at different rates, depending on their mobility within the drift gas and the strength of the electric field. The strength of the electric field is determined by the voltages applied first and final ring of the drift tube. Voltages applied to each section of the device are detailed in Sect. 4.2.2.4. Finally, separated ion packets pass through the mesh on the exit of the drift tube and produce a current on a Faraday plate electrode. For all IMS experiments discussed herein, an electric field strength of 226 V/cm was employed. A 2 mM equimolar mixture of TAA-Br salts in ACN was used to test the performance of the 3D printed IMS as TAA cations are often used as ion mobility standards. Their frequent use is the result of a low propensity to form clusters under a variety of conditions [40].

In traditional DT-IMS instruments, the time-scale for ion injection has been shown to have a noticeable effect on resolving power [27, 41]. Typically, DT-IMS instruments operated at atmospheric pressure employ an injection time ranging from 0.10 up to 1.0 ms. Increasing injection time has been shown to increase sensitivity, but the ability to separate peaks is degraded. Ion injection periods ranging from 0.3 to 1.0 ms were tested with the 3D printed IMS and the resulting spectra are shown in Fig. 4.6. In Fig. 4.6 the peaks correspond to TBAB, THAB,

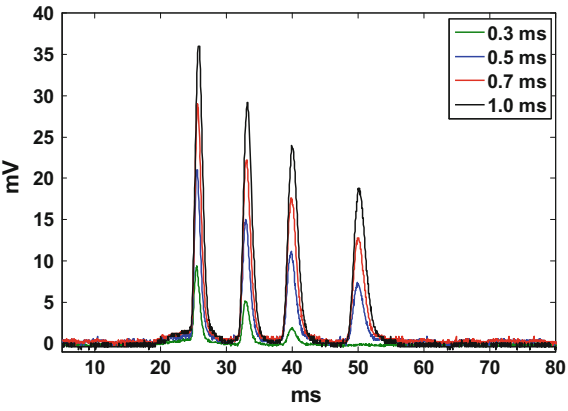

Fig. 4.6 Separation of 2 mM equimolar tetrabutyl-, tetrahexyl-, tetraoctyl-, and tetradodecylammonium cations under different injection times. Drift field strength was 226 V/cm and a 50 V injection potential (relative to first ring of drift tube) was used in all cases. Each spectrum is the resulting average of 16 scans at a 10 Hz acquisition rate

TOAB, and TDDAB cations, as labeled from left to right. 0.3 ms was the smallest time-scale tested for ion injection as no peak for the TDDAB cation was detected with the use of a 50 V injection potential. These results show the large sensitivity increases for longer injection times and the expected broadening associated with the sensitivity gain.

The performance of IMS instruments is often stated with respect to resolving power (R_p) [39]. R_p is calculated from the drift time (t_d) and full width of the peak at half maximum (FWHM) using Eq. 4.1:

$$R_p = \frac{t_d}{FWHM} \tag{4.1}$$

From the results shown in Fig. 4.6 the R_p for the tetrabutylammonium peak at an injection time period of 500 μs is calculated to be 25. Using an atmospheric pressure IMS of similar dimensions and operating conditions, Hill et al. measured R_p values ranging from 15 to 30 for methy tert-butyl ether (MTBE) ions when injection time periods were in the range of 300–500 μs [41]. This comparison shows that measured R_p from the 3D printed IMS are in the range achievable by traditional DT-IMS, and are in fact slight better than those attainable by most field-portable IMS instruments [42].

Another operational parameter effecting DT-IMS performance is the injection voltage for gating ions into the drift cell. Most commonly, ion gating in DT-IMS instruments is accomplished using a series of electrically isolated parallel wires, in the form of a Bradbury-Nielson [43], or Tyndall [44] shutter. When closed, inter-digitated wires have opposing potentials applied, thus ions are drawn to the wires rather than passing through. Ions are gated through the shutter by applying matching potentials to opposing wires, thus ions pass through as there is no electric field orthogonal to that supplied by the drift cell. An alternative manner of gating ions into a drift cell is the use of two parallel mesh electrodes [45]. In this case, ions are gated into the drift cell by increasing the potential on the back mesh, such that ions are pushed through openings in the mesh held flush with the drift cell. Alternatively, the potential on the first drift ring and mesh is briefly lowered, allowing ions to pass. In practice, this type of ion gate is much easier to construct and is more mechanically durable that ion shutters utilizing wires. There is however a trade-off with respect to efficiency. The openings in the mesh must be selected to balance transmission efficiency with durability as well as electrical shielding of the drift cell from perturbations by injection voltages.

Due to simplicity in construction, two parallel meshes were used to form the injection region in the 3D printed IMS as detailed in Sect. 4.2.2. In practice, it was found that optimal performance of the 3D printed IMS was using injection voltages in the range of 50–100 V. Beyond 100 V, no significant improvement in sensitivity was found. The resulting IMS spectra of the 2 mM equimolar TAA mix for different injection voltages and time periods is shown in Fig. 4.7. From these results it would initially appear that ion arrival times are altered by the injection time period; however, this is likely an artifact of detector timing. The start time of spectral

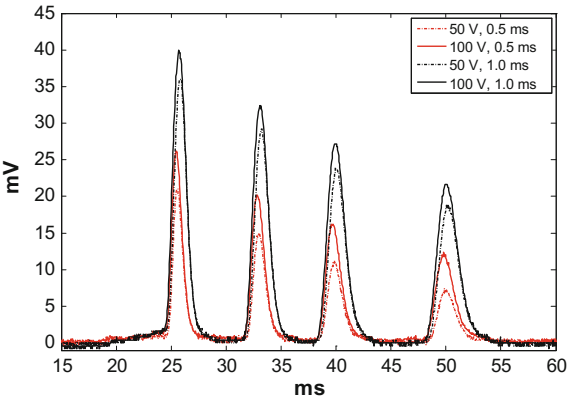

Fig. 4.7 IMS spectra of electrosprayed 2 mM equimolar mixture of tetrabutyl-, tetrahexyl-, tetraoctyl-, and tetradodecylammonium Br in ACN for different injection time periods and voltages. Injection voltage is given in reference to the potential on the first ring of the drift cell

collection is triggered on the rising-edge of the injection pulse, rather than centered on the injection waveform. A close comparison of the data in Fig. 4.7 verifies this phenomenon as peaks for the TAA cations are shifted by ~0.3 ms when comparing 1.0–0.5 ms injection, consistent with the previously stated hypothesis.

Another interesting trend observed is the decrease in intensities for longer drift times. This can partially be explained by peak broadening, however integration under each respective peak gives a decrease of 76, 71, and 56% for the THAB, TOAB, and TDDAB peak, respectively, from the total area under the peak from TBAB. Likely, the largest contributing factor to the decrease in intensity is the mobility of each cation. The less mobile cations (cations emerging at longer time scales) are not injected as efficiently by the method used herein. Because the ions must travel the separation distance between the two mesh electrodes, more of the ions with higher mobilities are injected than those displaying lower mobilities. This discrepancy can possibly be reduced in future instrument designs, by decreasing the distance between the injection mesh and the mesh held flush with the drift tube entrance.

The resolution of a DT-IMS is also affected by processes occurring within the drift cell itself. As an ion cloud traverses a drift cell, it is subject to expansion in both axial and radial directions by way of diffusion and space-charge effects. Space-charge effects can be mediated slightly by decreasing the injection time, but not without a loss of sensitivity. To combat the effect of axial expansion from both diffusion and space charge, higher electric field strengths can be used as this decreases the residency time within the drift cell. This is only effective to a certain extent as detailed by Siems et al. [39]. Radial expansion of the ion plume is also partially responsible for peak broadening within drift cell instruments. This is due to the non-uniformity of the electric field near the walls of the cell [39]. Previous work by Fernadez et al. has demonstrated that ion expansion within a 30 mm wide drift tube, in which ions produced by a corona discharge were gated into the drift tube and expanded radially ~2× along the 26 cm long drift region [27]. With the

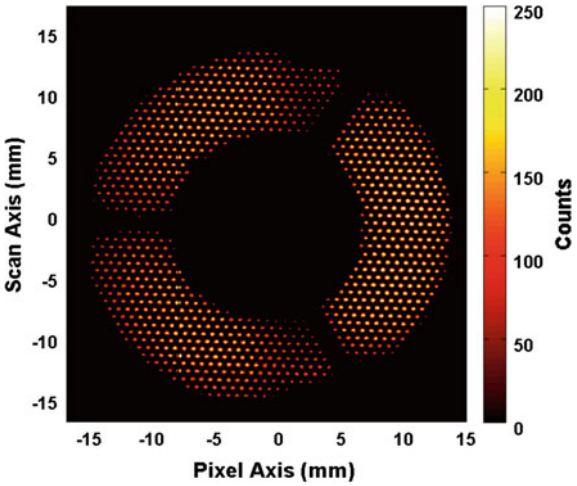

Fig. 4.8 Ion intensity map taken at exit of drift cell. Ions were generated by nanoESI from a 10 μM mixture of TBAB, THAB, TOAB, and TDDAB in ACN

traditional open-ring drift cell design, the influence of this is often reduced by using wider diameter drift rings and restricting ion injection to the center of the device.

Previous results suggest that the use of the annular focusing source under operational parameters herein should limit ion injection to a line width of ~500 μm, centered between the outer and central rings of the drift cell in the 3D printed IMS. To investigate the radial expansion of ions along the drift cell, an intensity map of ions exiting the drift cell was taken by removing the Faraday plate detector and scanning an IonCCD™ detector across the exit mesh of the drift cell as previously described. A solution of 10 μM of the same TAA mixture in ACN was used as the spray solvent and ions were continuously gated (ion gate held open at 50 V) into the drift cell. The resulting ion intensity map is shown in Fig. 4.8. From this image it is evident ions are rapidly expanding radially during drift cell transit. This image also illustrates the limited ion transmission by the 69% open stainless steel mesh, which likely decreases sensitivity significantly.

4.3.3 Ion Transmission Efficiency

The efficiency of ion transmission for both the annular focusing electrode, and the entire 3D printed IMS was investigated as described in Sect. 4.2.4. The total transmission efficiency of the annular focusing electrode for a range of deposition currents (varied by altering spray potential) under 3 different focusing potentials is shown in Fig. 4.9. A comparison of the data in Fig. 4.9 to that of Fig. 4.5 shows that up to 80% of nanoESI spray current can be deposited into a ~20 mm wide annulus with a line width of ~200 μm. Transmission efficiency of the 3D printed IMS under typical operating conditions was generally in the range of 0.8–1%.

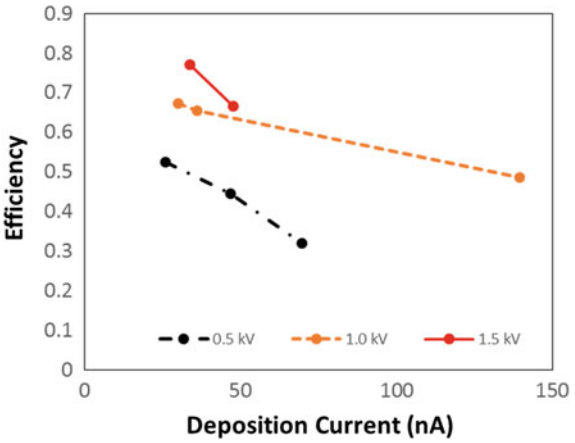

Fig. 4.9 Ion transmission efficiency of annular focusing electrode for a range of deposition currents at different focusing potentials. The potential applied to the annular focusing electrode is given in the figure legend. The spray solution was a 2 mM equimolar mixture of TBAB, THAB, TOAB, and TDDAB in ACN

As previously mentioned, this is likely due to large losses on the 3 stainless steel meshes, as well as minor losses to the walls of the drift tube from radial expansion of the ion plume.

4.4 Conclusions

A novel form of atmospheric pressure ion focusing was demonstrated in which up to 80% of electrosprayed ions from a nanoESI emitter are focused into an annulus with a line width of less than 200 μm FWHM. The annular focusing source was integrated with a fully 3D printable DT-IMS incorporating concentric ring electrodes operated at ambient pressure with no supplementary gas flow. A separation of electrosprayed TAA cations was demonstrated with a resolving power comparable to traditionally manufactured atmospheric pressure DT-IMS instruments. All mechanical components were manufactured by FDM, making this a low-cost, readily accessible means of constructing an IMS.

The ability to separate an electrosprayed mixture under ambient pressure and temperature may prove to be a valuable tool in the study of accelerated reaction in electrosprayed droplets. Normally, IMS instruments employ a desolvation region when coupled with electrospray sources, thus allowing for studies on the conformation and size of solvent-free ions. In the case of accelerated reactions in electrosprayed droplets [46, 47], it is of interest to study solvated ions and measure the properties of droplets with sizes too small to measure using techniques such as phase-Doppler anemometry (PDA). In such cases, it may be necessary to "freeze" droplets in their current state for analysis, by carrying out IMS separations in solvent-saturated vapors. Because of the inherent low-cost and speed at which the 3D printed instrument can be made, replacing IMS components that may become damaged by long-term and repeated solvent exposure is very economical (the

typical cost of FDM feedstock is typically less than $0.05/g). Additionally, a wide variety of thermoplastic feedstocks are available for purchase, and many more in development, thus material can be selected based on the application.

In light of these potential applications, there remains a significant amount of work to be done, towards understanding IMS separations occurring under such unique conditions. A good understanding of the fundamentals of ion migration through these complex media under electric fields is necessary to infer physical properties from the measured data. Moreover, improvements in the separation power and sensitivity of this type of ion mobility drift cell must be made in order to further the usefulness of this design. In particular, transmission efficiency may be improved by taking better advantage of the annular focusing nature of the source region. In the current design, the greatest sensitivity in IMS separations was accomplished with the least amount of annular focusing. This is likely the result of the stainless steel meshes, as ions have a larger probability to pass through the mesh openings when spread over a large area. This effect may be mitigated by replacing the mesh with an electrode containing a single open slit, in the form of a ring. By precisely aligning this slit with the focal region a larger injection efficiency is expected. Furthermore, ions would be restricted to injection only in the most uniform region of the electric field, thus simultaneously improving the resolution of ion separation.

References

1. M.J. Cohen, F.W. Karasek, J. Chromatogr. Sci. **8**, 330–337 (1970)
2. H.E. Revercomb, E.A. Mason, Anal. Chem. **47**, 970–983 (1975)
3. F.W. Karasek, Anal. Chem. **46**, 710A–720A (1974)
4. D.F. Hagen, Anal. Chem. **51**, 870–874 (1979)
5. R.G. Ewing, D.A. Atkinson, G.A. Eiceman, G.J. Ewing, Talanta **54**, 515–529 (2001)
6. G.A. Eiceman, E.V. Krylov, N.S. Krylova, E.G. Nazarov, R.A. Miller, Anal. Chem. **76**, 4937–4944 (2004)
7. G. Reid Asbury, J. Klasmeier, H.H. Hill Jr., Talanta **50**, 1291–1298 (2000)
8. G.A. Eiceman, J.A. Stone, Anal. Chem. **76**, 390A–397A (2004)
9. W.E. Steiner, B.H. Clowers, L.M. Matz, W.F. Siems, H.H. Hill, Anal. Chem. **74**, 4343–4352 (2002)
10. B.M. Kolakowski, Z. Mester, Analyst **132**, 842–864 (2007)
11. B.C. Bohrer, S.I. Merenbloom, S.L. Koeniger, A.E. Hilderbrand, D.E. Clemmer, Annu. Rev. Anal. Chem. **1**, 293–327 (2008)
12. C. Uetrecht, R.J. Rose, E. van Duijn, K. Lorenzen, A.J.R. Heck, Chem. Soc. Rev. **39**, 1633–1655 (2010)
13. B.T. Ruotolo, J.L.P. Benesch, A.M. Sandercock, S.-J. Hyung, C.V. Robinson, Nat. Protocols **3**, 1139–1152 (2008)
14. C.J. Hogan, B.T. Ruotolo, C.V. Robinson, J. Fernandez de la Mora, J. Phys. Chem. B **115**, 3614–3621 (2011)
15. G.A. Eiceman, Z. Karpas, H.H. Hill Jr., in *Ion Mobility Spectrometry,* 3rd edn. (CRC Press, Editon edn., 2013), pp. 1–20
16. A.B. Kanu, P. Dwivedi, M. Tam, L. Matz, H.H. Hill, J. Mass Spectrom. **43**, 1–22 (2008)

17. T. Wyttenbach, M. Bowers, in *Modern Mass Spectrometry*, vol. 225, ed. by C. Schalley (Springer, Berlin Heidelberg, Editon edn., 2003), pp. 207–232
18. G.A. Eiceman, Z. Karpas, H.H. Hill Jr., in *Ion Mobility Spectrometry,* 3rd edn. (CRC Press, Editon edn., 2013), pp. 119–153
19. R. Cumeras, E. Figueras, C.E. Davis, J.I. Baumbach, I. Gracia, Analyst **140**, 1376–1390 (2015)
20. R. Guevremont, J. Chromatogr. A **2004**, 3–19 (1058)
21. P.F. DeCarlo, J.G. Slowik, D.R. Worsnop, P. Davidovits, J.L. Jimenez, Aerosol Sci. Technol. **38**, 1185–1205 (2004)
22. R.C. Flagan, Aerosol. Sci. Technol. **28**, 301–380 (1998)
23. R.W. Purves, R. Guevremont, S. Day, C.W. Pipich, M.S. Matyjaszczyk, Rev. Sci. Instrum. **69**, 4094 (1998)
24. J.F. de la Mora, L. de Juan, T. Eichler, J. Rosell, TrAC Trends Anal. Chem. **17**, 328–339 (1998)
25. I.A. Buryakov, E.V. Krylov, E.G. Nazarov, U.K. Rasulev, Int. J. Mass Spectrom. Ion Processes **128**, 143–148 (1993)
26. S. Chapman, Phys. Rev. **52**, 184–190 (1937)
27. M. Kwasnik, K. Fuhrer, M. Gonin, K. Barbeau, F.M. Fernández, Anal. Chem. **79**, 7782–7791 (2007)
28. G.A. Eiceman, Z. Karpas, H.H. Hill, *Ion Mobility Spectrometry*, 3rd edn. (Taylor and Francis, Hoboken, 2013)
29. K. Giles, S.D. Pringle, K.R. Worthington, D. Little, J.L. Wildgoose, R.H. Bateman, Rapid Commun. Mass Spectrom. **18**, 2401–2414 (2004)
30. A.A. Shvartsburg, R.D. Smith, Anal. Chem. **80**, 9689–9699 (2008)
31. Y. Zhong, S.-J. Hyung, B.T. Ruotolo, Analyst **136**, 3534–3541 (2011)
32. J. Rosell-Llompart, I.G. Loscertales, D. Bingham, J. Fernández de la Mora, J. Aerosol Sci. **27**, 695–719 (1996)
33. E.A. Mason, E.W. McDaniel, in *Transport Properties of Ions in Gases* (Wiley-VCH Verlag GmbH & Co. KGaA, Editon edn., 2005), pp. 137–193
34. D. Smith, T. Knapman, I. Campuzano, R. Malham, J. Berryman, S. Radford, A. Ashcroft, Eur. J. Mass Spectrom. **15**, 113–130 (2009)
35. T.W. Knapman, J.T. Berryman, I. Campuzano, S.A. Harris, A.E. Ashcroft, Int. J. Mass Spectrom. **298**, 17–23 (2010)
36. Z. Baird, W.-P. Peng, R.G. Cooks, Int. J. Mass Spectrom. **330–332**, 277–284 (2012)
37. Z. Baird, P. Wei, R.G. Cooks, Analyst **140**, 696–700 (2015)
38. S. YD, in *Mathworks* (MATLAB Central File Exchange, Editon edn., 2013)
39. W.F. Siems, C. Wu, E.E. Tarver, H.H. Hill Jr., P.R. Larsen, D.G. McMinn, Anal. Chem. **66**, 4195–4201 (1994)
40. J. Viidanoja, A. Sysoev, A. Adamov, T. Kotiaho, Rapid Commun. Mass Spectrom. **19**, 3051–3055 (2005)
41. A.B. Kanu, M.M. Gribb, H.H. Hill, Anal. Chem. **80**, 6610–6619 (2008)
42. A.B. Kanu, P.E. Haigh, H.H. Hill, Anal. Chim. Acta **553**, 148–159 (2005)
43. N.E. Bradbury, R.A. Nielsen, Phys. Rev. **49**, 388–393 (1936)
44. A.M. Tyndall, C.F. Powell, in *Proceedings of the Royal Society of London. Series A, Containing Papers of a Mathematical and Physical Character*, vol. 134, pp. 125–136 (1931)
45. United States Pat., 5,200,614 (1993)
46. T. Müller, A. Badu-Tawiah, R.G. Cooks, Angew. Chem. Int. Ed. **51**, 11832–11835 (2012)
47. M. Girod, E. Moyano, D.I. Campbell, R.G. Cooks, Chem. Sci. **2**, 501–510 (2011)

Chapter 5
Outlook and Future Directions

5.1 3D Printing in the Scientific Laboratory

5.1.1 Overview of FDM Printers and Components

While a brief introduction to the FDM process was provided in Sect. 1.4, a more detailed overview of the components, kinematics, and figures of merit of different types of 3D printers is warranted. In general, a 3D printer must include: (i) a platform on which the object is to be built, (ii) a means of additive delivery of material in a controlled manner, and (iii) accurate and precise control of positioning in at least 3 axes. These requirements can be addressed by several approaches with trade-offs in cost and performance. For the sake of brevity, only FDM printers will be covered within this chapter.

The build-surface provides the literal base on which any 3D printed part is manufactured. Though not required for some materials, this platform is most-often temperature controlled with typical settings ranging from 45 to 120 °C depending on the material being printed. Heating of the platform improves adhesion to the surface as well as promotes even cooling of the part throughout the process, thus limiting warping of the part. Perhaps the simplest and most common method of providing heat to the platform is through resistive heating by passing a relatively high current through a series of copper traces on a printed circuit board (PCB) [1]. Providing heat in this manner allows for the use of DC voltages and current control via a circuit employing a MOSFET as a switch. This type of heating is most effective over build areas smaller than 200 × 200 cm. Larger platforms necessitate the use of heating pads which run off of AC voltages to provide much faster heating times (even for very large build surfaces) but must be controlled by a solid state relay (SSR) and are inherently more dangerous as the voltage range in which they operate is potentially fatal if mishandled.

As previously stated, a heated build surface is not always necessary; however, there are 2 main requirements for any surface on which plastic will be deposited for

Z. Baird, *Manipulation and Characterization of Electrosprayed Ions Under Ambient Conditions*, Springer Theses, DOI 10.1007/978-3-319-49869-0_5

a 3D printed part. First, the surface must be flat to ensure that the thickness of material deposition on the first layer is consistent. Flatness is most easily realized by printing onto a sheet of glass. A typical arrangement is to stack the glass on top of the heater, often with an aluminum sheet in between to distribute heat more evenly. Second, the plastic to be deposited must adhere to the surface throughout the entire print, yet still allow for object to be removed from the bed upon completion. The use of a heated bed has an advantage in this respect, as adhesion is stronger at a correctly selected temperature and contraction of the bed upon cooling allows for the part to be removed with relative ease. Because not all plastic adheres well to glass alone, the surface is often coated with polyvinyl alcohol (PVA) based glues, acetone/ABS slurries, blue painters tape, and even hairspray. Recently there have been a number of products marketed specifically for bed treatment that are compatible with most commonly used plastics. These include BuildTak (an adhesive-backed, textured plastic sheet), 3D-EEZ, and polyetherimide (PEI) sheets, to name a few. There is no one-size-fits-all solution for bed treatment, and as such empirical testing is the normal approach for finding the correct solution for new materials. For applications of 3D printing specifically within the fields of chemistry it is important to consider the contaminants that may be introduced by different bed treatments and select an appropriate method, accordingly.

The precise delivery and deposition of material in FDM 3D printers is a concerted effort that relies on 2 components, the extruder and hot end. Extruders form the basis for volumetric material delivery by pushing a plastic filament of known diameter into the hot end. Within the hot end, the plastic is melted in a controlled zone (the melt zone) immediately prior to deposition through the nozzle orifice. The width of the orifice, the vertical positioning of the nozzle, movement speed, and the volumetric delivery of material all serve to define the layer height and extrusion width of the line of plastic that is extruded. As the extruder is responsible for controlling the rate at which material is delivered, this is perhaps the most critical aspect of achieving dimensionally accurate parts (aside from positioning error). The most common method of controlling the flow rate is to push a plastic filament of known diameter with a drive gear (or set of drive gears), the rotation of which is controlled by a stepper motor. There are a multitude of extruders and drive gear designs to select from and an ideal extruder grips the filament as well as possible while avoiding deformation, provides high torque, and allows the plastic filament to be pushed at a relatively fast linear speed.

The second component responsible for material deposition is often referred to as the hot end, due to its use of heat to transform the solid plastic feedstock into a free-flowing material that will bond to the previous layer upon exiting the nozzle. There are many different hot end assemblies available for purchase, but each functions in a nearly identical manner. In general, the plastic filament is pushed along a straight cylindrical channel capped with a metal nozzle. Heating of the filament is restricted to the region closest to the nozzle in order to limit expansion of the plastic in the constrained channel and to better control the flow of liquid from the nozzle (limit the melt zone). Some hot ends are specifically designed with a longer than average melt zone in order to achieve faster print speeds. Thermal

conductivity of most plastics is generally quite low so careful control of print speeds and temperatures is necessary to achieve consistent quality within a 3D printed object.

There are 2 common ways of arranging an extruder and hot end in order to deliver plastic to the build surface: direct-drive, and the so-called Bowden arrangement. In a direct-drive setup the drive gears are located as close to the entrance of the hot end assembly as possible so as to eliminate backlash when performing retraction and prime movements. This makes for very short retraction distances and time periods and allow for the filament to be fully constrained from the time it enters the drive gears of the extruder and is melted by the hot end. The adverse effect arising from this particular arrangement is the amount of weight this adds to the print head, thus slowing the maximum effective print speed and acceleration that can be used for positioning. This is particularly troublesome for printers with large build volumes as longer belts introduce more play into the system. The Bowden arrangement allows for a much lower print head weight by locating the extruder in a stationary position, distal from the other moving components of the system. In a Bowden extruder the filament is fed into a hollow tube with an inner diameter closely matching that of the filament and the other end is coupled to the hot end. As a trade-off, Bowden extrusion systems exhibit much more backlash due to the tension of the tube, play within tube coupling components, and slight mismatch of filament and tube diameter. Because of this, Bowden extruders are more difficult to calibrate in order to maximize print quality.

Along with precise material delivery, accurate and precise positioning of the deposited plastic is critical to the production of a 3D printed object with good dimensional tolerance. There are a number of different kinematic systems employed in 3D printers, and a full discussion of this is beyond the scope of the present text as most of these systems are well-known and employed in a variety of robotic systems. For the purpose of this discussion it is sufficient to note that most, if not all, proven FDM systems rely on stepper motors, timing belts, and pulleys to realize computer numerical control (CNC) of the deposition of plastic in FDM.

5.1.2 Notable Applications of FDM

The recent boom experienced in the 3D printing industry, namely that of FDM technology, provides an opportunity for research laboratories to harness the capabilities of these methods. The low entry cost, combined with cheap and widely available materials makes this an appealing tool for a variety of different uses. The majority of the work discussed in this dissertation has dealt with the application of FDM to the control of ions under atmospheric pressures, yet it is imperative to consider other ways in which additive manufacturing can influence work performed in research laboratories. While not discussed within the context of this work 3D printed components have filled vital roles within the entire scope of my research interests. Any scientific laboratory is stocked with specialized equipment and

instrumentation. Such instruments often require home-built fittings, brackets, etc. that may be produced cheaply and on-demand by additive manufacture. However, many scientific applications involve exposure of parts to extreme conditions such as temperature fluctuations, tissue growth media, solvent systems, and even ionizing radiation, conditions not often suitable for traditional thermoplastics.

With the consumer and hobbyist adoption of FDM 3D printing technology a new market has been realized for production and distribution of unique and specialized materials that are available at relatively low cost. Furthermore, there are open-source filament extruders that can be purchased/built which allow for the production of materials that are not available for purchase [2].

Thermoplastic elastomers (TPE) describe a fairly broad range of materials that are most generally referred to as "flexible" materials, due to their elastomeric properties. Because of their inherent flexibility, TPE materials are particularly well-suited for tissue engineering applications where connectivity must be retained while the material undergoes stress and displacement. Several cases have been demonstrated in which a printed TPE scaffold was used as a support structure for tissue growth [3–5].

The production of application-derived materials suitable as feedstock for FDM is not always straightforward, often requiring extensive testing and modification for optimal performance. Because of this, it is often more feasible to simply modify the surface of a traditional thermoplastic for compatibility with its planned usage. Surface modification to achieve biocompatibility of 3D printed ABS (one of the most common and versatile FDM feedstocks) was recently demonstrated by McCollough et al. Through surface treatment of printed ABS they were able to reduce non-specific protein binding as well as increase biocompatibility [6]. These modifications serve to improve the performance of 3D printed microfluidic devices, a field which has shown rapid growth in recent years [7]. These 2 examples highlight just some of the possibilities that FDM can provide in the development of new medical devices and diagnostic platforms.

Another challenge faced in the manufacture of parts by FDM is the geometric constraints regarding free-hanging artifacts, otherwise known as overhangs. These features lack the base on which a layer of plastic can be deposited and therefore support structures can be employed. Support structures can be printed to simply break away from the part once completed, but this can leave undesirable surface artifacts. Alternatively, through the use of dissolvable support material, such as PVA the support structures can be easily removed by soaking the object in a solvent [8].

5.2 Ion Focusing at Atmospheric Pressure

The work presented in chapters two through four of this dissertation show examples of different ways in which ions may be manipulated in the air at atmospheric pressures. As discussed in Sects. 1.1 and 1.3, the motion of ions under these

conditions is complicated as the result of collisions, droplet desolvation, and space-charge effects. As such, control of the ions' trajectories requires a non-traditional approach. I have sought to explore a combined tactic of simulations and experiments with rapid prototyping that may be applied to gain an understanding of how unconventional electrode geometries can be used to facilitate control of ion clouds generated by electrospray. These experiments serve only as proof-of-concepts, as more effort must be given to optimize geometries, and gain a better understanding of the phenomena in general. Notably, plastic electrodes produced in this manner have high porosity thus solvent adsorption onto walls and resulting plastic solvation effects must be considered. This is especially important if these electrodes are to be used for long-term applications.

Perhaps the most profound effect discovered by these methods is the annular focusing of electrosprayed ions as discussed in Chap. 4. Compared to the use of the more conventional open-channel electrodes, this design is highly efficient at spatially focusing ions, while blocking the passage of large solvent droplets. In order for the annular focused ions to be detected by MS an efficient method of introducing annular ion clouds into a vacuum system must be developed. Perhaps the most probable method of doing so is by employing an MS inlet in the form of a conical slit, this concept is shown in Fig. 5.1. Experiments with this design must be done to verify that gas flow in this type of vacuum system interface would generate sufficient drag forces to carry ions into the reduced pressure environment. The converging nature of this design, coupled with the large pressure drop across the system makes estimating the flow from first principles or numerically, both challenging approaches. Empirical exploration of this type of inlet system is relatively straightforward, so long as it is possible to effectively manufacture a design of this type.

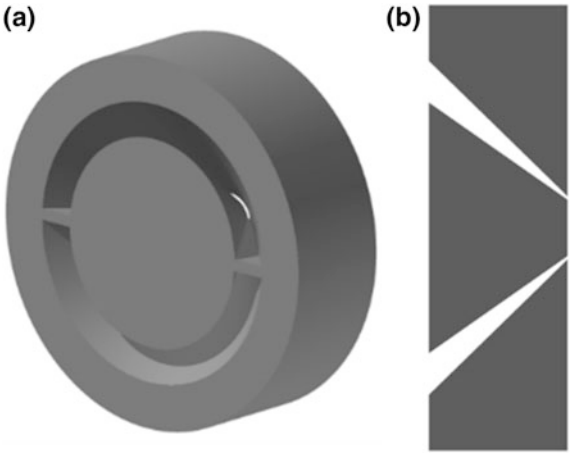

Fig. 5.1 Concept design of an alternative atmospheric pressure interface for coupling with an annularly focusing ion source **a** and a cross-section of the concept inlet **b**

5.3 Ambient Ion Mobility Spectrometry

While differential mobility analysis (DMA), field asymmetric waveform ion mobility spectrometry (FAIMS), and traditional embodiments of drift tube ion mobility spectrometry (DT-IMS) are capable of operation at atmospheric pressure, in current forms, each has limitations if considered for ambient analysis of droplets and solvated ions. In this case, ambient means droplets and ions in a stable equilibrium with their environment, that is, no significant evaporation or ongoing desolvation. The analysis of droplets and ions in this state is of critical importance in understanding the factors contributing to accelerated reactions and general ion formation occurring within an electrospray plume. Tandem DMA is the most obvious method of performing such analysis as this has previously been demonstrated for studies on aerosol growth and nucleation [9, 10]. DMA measurements have even been used to study the ion evaporation model (IEM) within electrosprayed droplets <3 nm [11, 12]; however these studies are limited by the range of the DMA which must be designed for measurements within specific particle sizes. Additionally, tandem DMA instruments in particular are instrumentally complex in nature, require precise control of gas flow, and the fundamentals of aerosol transfer within and between individual DMAs must be well understood to interpret the results of such experiments.

The disposability and cost-effectiveness of instruments employing 3D printed components makes them amenable to use in harsh environments such solvent-saturated gas environments necessary to halt the evaporation of droplets. Through extensions of the work presented in this dissertation it is hoped that new, relatively low cost, and modular instrumentation will be developed to allow for analysis of solvated clusters and nanometer size droplets to be measured in a rapid and ambient manner. From these measurements it may be possible to gain a better understanding of reaction acceleration within electrosprayed droplets.

References

1. J. Průša, *PCB Heatbed*, http://reprap.org/wiki/PCB_Heatbed. Accessed 19 May 2016
2. C. Baechler, M. DeVuono, J.M. Pearce, Rapid Prototyping J. **19**, 118–125 (2013)
3. T.B.F. Woodfield, J. Malda, J. de Wijn, F. Péters, J. Riesle, C.A. van Blitterswijk, Biomaterials **25**, 4149–4161 (2004)
4. J. Korpela, A. Kokkari, H. Korhonen, M. Malin, T. Närhi, J. Seppälä, J. Biomed. Mater. Res. Part B: Appl. Biomater. **101B**, 610–619 (2013)
5. V. Liu, Tsang and S. N. Bhatia. Adv. Drug Deliv. Rev. **56**, 1635–1647 (2004)
6. E.J. McCullough, V.K. Yadavalli, J. Mater. Process. Technol. **213**, 947–954 (2013)
7. C.M.B. Ho, S.H. Ng, K.H.H. Li, Y.-J. Yoon, Lab Chip **15**, 3627–3637 (2015)
8. C. Duran, V. Subbian, M.T. Giovanetti, J.R. Simkins, F.R.B. Jr, Rapid Prototyping J. **21**, 528–534 (2015)
9. M.J. Cubison, H. Coe, M. Gysel, J. Aerosol Sci. **36**, 846–865 (2005)

10. L. Wang, A.F. Khalizov, J. Zheng, W. Xu, Y. Ma, V. Lal, R. Zhang, Nat. Geosci. **3**, 238–242 (2010)
11. C.J. Hogan Jr., J. Fernandez de la Mora, PCCP **11**, 8079–8090 (2009)
12. M. Gamero-Castaño, J.F.d.l. Mora, J. Mass Spectrom. **35**, 790–803 (2000)

Curriculum Vitae

Zane Baird was born and spent his childhood in northern Utah. He received his BSc. in Chemistry from Southern Utah University (SUU) in 2010. It was at SUU under the guidance of Dr. Renwu Zhang that Zane gained his first research experience, studying the free-volume distribution within poly(trimethylsilyl)propyne through the use of positron annihilation lifetime spectroscopy (PALS). Zane was also employed as an analyst at the SUU Waterlab for 2 years during his studies under the supervision of Dr. Kim Weaver. In the summer of 2009 he spent time in the lab of Dr. Abraham Clearfield at Texas A&M University performing undergraduate research relating to the use of antimony silicate pyrochlores in nuclear waste remediation. In the fall of 2010 Zane began his doctoral studies under the direction of Dr. R. Graham Cooks at Purdue University. In the summer of his second year Zane spent 1 month at Tsinghua University in Beijing, China. There he served as a teaching assistant for a course on mass spectrometry taught by a group of professors from Purdue University, Ohio University, the Ohio State University, and University of Wisconsin-Madison. Throughout his time in the labs of Dr. R. Graham Cooks Zane contributed to research in many areas including atmospheric pressure ion focusing, intraoperative cancer diagnostics, crystallization in droplet and thin films, nanoparticle synthesis, as well as ion mobility spectrometry. Zane has published two first author peer-reviewed articles and presented his research at numerous conferences. In addition, Zane worked towards the incorporation of fused deposition modeling (FDM), a 3D printing technique, into many aspects of work within the laboratory. Zane was a member of the Phi Lamba Upsilon (PLU) honor society and the American Society for Mass Spectrometry (ASMS) for each of his years at Purdue. Zane was also a founding officer of Purdue's 3D Printing Club, where he designed several models for fundraising projects.

Z. Baird, *Manipulation and Characterization of Electrosprayed Ions Under Ambient Conditions*, Springer Theses, DOI 10.1007/978-3-319-49869-0